

# Higgs-mode resonance in third harmonic generation in NbN superconductors: Multiband electron-phonon coupling, impurity scattering, and polarization-angle dependence

Naoto Tsuji<sup>1</sup> and Yusuke Nomura<sup>1</sup>

<sup>1</sup>*RIKEN Center for Emergent Matter Science (CEMS), Wako 351-0198, Japan*

(Dated: October 9, 2020)

We theoretically investigate the resonance of third harmonic generation (THG) that has been observed at frequency being half of the superconducting gap in a multiband disordered superconductor NbN. The central question is whether the dominant contribution to the THG resonance comes from the Higgs mode (the collective amplitude mode of the superconducting order parameter) or quasiparticle excitations. To resolve this issue, we analyze a realistic three-band model with effective intraband and interband phonon-mediated interactions together with nonmagnetic impurity scatterings. Using the first principles estimate of the ratio between the intraband and interband pairing interactions with multiband impurity scattering rates being varied from clean to dirty regimes, we calculate the THG susceptibility for NbN in a channel-resolved manner by means of the BCS and self-consistent Born approximations. In the dirty regime, which is close to the experimental situation, the leading contribution is given by the paramagnetic channel of the Higgs mode having almost no polarization-angle dependence, while the second leading contribution comes from the paramagnetic channel of quasiparticles generally showing significant polarization-angle dependence. The result is consistent with the recent experimental observation of no polarization-angle dependence of THG, giving firm evidence that the Higgs mode dominantly contributes to the THG resonance in NbN superconductors.

## I. INTRODUCTION

The standard microscopic theory of superconductivity, i.e., the BCS theory, predicts the presence of the collective amplitude mode of the superconducting order parameter [1–6], which is recently referred to as the Higgs mode due to the close analogy with the Higgs boson in particle physics (for recent reviews, see [7, 8]). Despite the fundamental and universal aspects of the Higgs mode, its observation in ordinary superconductors had been elusive until recently. One exception was a superconductor  $2H\text{-NbSe}_2$ , which is special in the sense that superconductivity and charge density wave (CDW) coexist in a single material. In this particular situation, the Higgs mode becomes Raman active, and has been observed in the early stage by Raman experiments [9, 10] (see also [11–13] for recent studies). However, the Higgs mode itself should exist irrespective of the presence of CDW, so that its observation in superconductors without any other orders has been long awaited.

The difficulty in observing the Higgs mode in superconductors without other coexisting orders is that the Higgs mode does not linearly couple to external electromagnetic fields, and that the energy of the Higgs mode, which lies around the superconducting gap energy  $2\Delta$ , is in the terahertz (THz) frequency range, for which an intense light source had been lacking for a long time. The recent development of THz laser techniques, however, has made it possible to excite the Higgs mode directly through the nonlinear light-Higgs coupling [14]. In fact, coherent oscillation of the superconducting order parameter with frequency  $2\Delta$  after irradiation with a monocycle THz pulse has been observed in a superconducting NbN [15]. Sub-

sequently, resonant enhancement of third harmonic generation (THG) at the condition of  $2\Omega = 2\Delta$  with  $\Omega$  being the incident light frequency has been reported for NbN using multicycle THz pulses [16].

While all these measurements are consistent with the interpretation that the Higgs mode is excited by THz laser excitations, it is not sufficient to confirm that the mode energy is  $2\Delta$ , since the pair-breaking energy of quasiparticles is also equal to  $2\Delta$ . This forces one to distinguish the collective Higgs mode from individual excitations of quasiparticles by properties other than the mode energy.

One way to discriminate them is to measure the polarization-angle dependence of the resonant THG [17]. According to the BCS mean-field calculation in the clean limit for a single-band model, the quasiparticle contribution has strong angle dependence in THG, whereas the Higgs-mode contribution does not. Followed by the theoretical proposal, the polarization-resolved measurement of THG has been performed for a single-crystal NbN, showing that the THG intensity at the resonance has almost no polarization-angle dependence [18]. Does this mean that the origin of the resonant THG observed in NbN is the Higgs mode?

The story is not so simple, because the BCS clean limit calculation also suggests that the absolute magnitude of the quasiparticle contribution to the THG resonance is generally much larger than that of the Higgs mode in the BCS clean limit [8, 17]. Considering both the polarization-angle dependence and absolute magnitude of the Higgs and quasiparticle contributions to the THG, we come to the conclusion that at least the BCS mean-field treatment in the clean limit fails to describe the THG experiments for NbN superconductors.

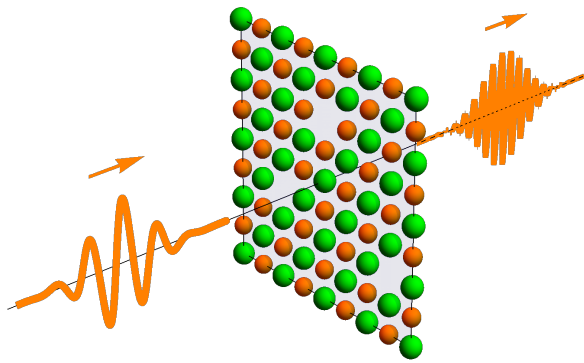


FIG. 1. A schematic picture of third harmonic generation in NbN superconductors with disorders or impurities (for which we illustrate lattice defects as an example).

There are several possibilities to circumvent this controversial situation: One is to go beyond the BCS approximation and include, e.g., phonon retardation effects. In fact, NbN is known to have a moderately strong electron-phonon coupling (with a dimensionless coupling constant  $\lambda \sim 1$ ) [19–21]. Based on the nonequilibrium dynamical mean-field theory [22], it has been shown that the Higgs mode can contribute to THG with an order of magnitude comparable to quasiparticles [23].

Another possibility is to depart from the clean limit and consider the effect of disorders or impurity scattering. Since the optical conductivity of NbN used in the THz laser experiments agrees well [15, 16] with the Mattis-Bardeen form [24], the NbN samples are close to the dirty limit. The effect of impurity scattering on THG in BCS superconductors has been studied in Refs. [25–27]. Strikingly, in the dirty regime the magnitude of the Higgs-mode contribution to THG can exceed by far that of quasiparticles.

These studies suggest that impurity scattering has more substantial effects on the magnitude of the THG resonance than phonon retardation. It is natural to expect so, because the impurity scattering rate generally approaches a nonzero constant value in the low-energy limit, while the electron-phonon scattering rate decays to zero in the Fermi-liquid regime. Hence, in the present study we focus on the effect of impurity scattering. A crucial key to the open issue of which of the Higgs mode or quasiparticles are dominant in the THG resonance in NbN is the polarization-angle dependence of THG in the dirty regime of superconductors, which has not been addressed so far.

In this paper, we study the polarization-angle dependence of THG in NbN superconductors with disorders (Fig. 1). For this purpose, we use an effective three-band model including the phonon-mediated multiband pairing interactions for NbN. In particular, we take special care of the relative magnitude between the intraband and interband pairing interactions, since the polarization-angle dependence might be strongly affected by it. In the

previous study [18], the calculations of the polarization-angle dependence for the three-band model have been performed at the BCS clean limit without first-principles estimate of the pairing interactions. The calculations assuming the same amplitude of the intraband and interband pairing interaction have shown that the Higgs-mode contribution in THG is isotropic, while the quasiparticle contribution has significant angle dependence [18]. For other choices of the relative magnitude between the intraband and interband interaction parameters, the Higgs mode can also exhibit the polarization-angle dependence [28]. In the present study, we go beyond these previous studies by taking into account the effect of impurities with a realistic estimate of the ratio between the intraband and interband interactions.

We first estimate the pairing interaction parameters for NbN from first principles calculations of the phonon band structure and the electron-phonon couplings. Using the estimated ratio between the intraband and interband interaction parameters, we calculate the THG susceptibility for the multiband superconductor NbN within the BCS mean-field theory. The effect of nonmagnetic impurity scattering is treated by means of the self-consistent Born approximation. We consider both intraband and interband impurity scatterings for multiband NbN superconductors. The calculated THG susceptibility is classified according to the physical origin (quasiparticle or Higgs mode), the coupling channel to light (diamagnetic or paramagnetic), and the diagrammatic representation in the presence of impurities.

The results show that the THG resonance is dominated by the paramagnetic channel in the dirty regime in NbN, in which the Higgs-mode contribution generally becomes larger than the quasiparticle contribution. This behavior is similar to the previous results for single-band superconductors [25, 27]. With the estimated ratio between the intraband and interband pairing interactions, the quasiparticles always show clear polarization-angle dependence of THG, while the Higgs mode does not in general, except in the vicinity of the parameter region where the interband impurity scattering rate vanishes. By comparing with the polarization-resolved THG measurements for NbN [18], we conclude that the dominant contribution to the THG resonance is coming from the Higgs mode rather than quasiparticles.

The paper is organized as follows. In Sec. II, we evaluate the electron-phonon couplings and the effective pairing interactions in NbN from first principles calculations. In Sec. III, we describe the method to calculate the THG susceptibility using an effective three-band model for NbN with multiband pairing interactions and impurity scatterings. In Sec. IV, we show the numerical results for THG in NbN superconductors, focusing on its magnitude and polarization-angle dependence of the Higgs-mode and quasiparticle contributions for various impurity scattering rates. The paper is summarized in Sec. V.

## II. FIRST PRINCIPLES ESTIMATION OF THE ELECTRON-PHONON COUPLING IN NbN

In this section, we evaluate the intraband and interband effective pairing interactions of NbN from first principles, which are important to determine the polarization-angle dependence of THG in multiband NbN superconductors as discussed in the introduction. The electronic band structure of NbN has been calculated from first principles in the previous literatures [18, 29–32]. The *ab initio* estimate of the phonon band structure and the electron-phonon coupling constant of NbN has been reported in [33–36]. While the total effective pairing interaction (summed over the band indices) has been derived in the previous calculations, here we need the band-resolved matrix elements of the pairing interaction.

Our approach is based on the *ab initio* construction of a low-energy effective model of NbN including the electron-phonon coupling. To this end, we perform the density functional calculation for NbN using QUANTUM ESPRESSO package [37, 38]. We use the Troullier-Martins norm-conserving pseudopotentials [39] in the Kleinman-Bylander representation [40] with the Perdew-Burke-Ernzerhof [41] exchange-correlation functional. We set the cutoff energy for the wave functions and charge density to be 100 eV and 400 eV, respectively, and take  $N_{\mathbf{k}} = 8 \times 8 \times 8$   $\mathbf{k}$  points for electron's momentum mesh.

The phonon band structure and the electron-phonon coupling constants are evaluated by the density functional perturbation theory [42], for which we use  $N_{\mathbf{q}} = 8 \times 8 \times 8$   $\mathbf{q}$  points for phonon's momentum mesh. The previous phonon band calculation [34, 35] shows that NbN in the NaCl-type structure has a structural instability as indicated by imaginary phonon frequencies, which is, however, not observed in experiments. To avoid such an instability, we employ a virtual crystal approximation, where we create a pseudopotential for Nb with the nuclear charge  $Z = +40.5$ . With this, we fully optimize the lattice structure, obtaining the lattice constant  $a = 4.497$  Å, which agrees well with the experimental data [43].

Our calculation of the electronic band structure of NbN (red curves in Fig. 2) well reproduces the previous results [18, 29–32]. Near the Fermi energy, there are three bands consisting of Nb's  $4d$   $t_{2g}$  orbitals ( $xy$ ,  $yz$  and  $zx$ ), which are occupied by two electrons in one unit cell in average. Therefore, NbN can be effectively regarded as a three-band system at one third filling at low energy. We first construct the effective three-band tight-binding Hamiltonian on the basis of the maximally localized Wannier orbitals [44, 45], for which we use the open-source package RESPACK [46]. We can simplify the effective three-band model by taking the leading hopping processes [18],

$$H_{\text{el}} = \sum_{\mathbf{k}n\sigma} \epsilon_{\mathbf{k}n} c_{\mathbf{k}n\sigma}^\dagger c_{\mathbf{k}n\sigma} \quad (n = xy, yz, zx), \quad (1)$$

where  $c_{\mathbf{k}n\sigma}^\dagger$  is a creation operator of electrons with momentum  $\mathbf{k}$ , orbital  $n$ , and spin  $\sigma$ . The simplified energy

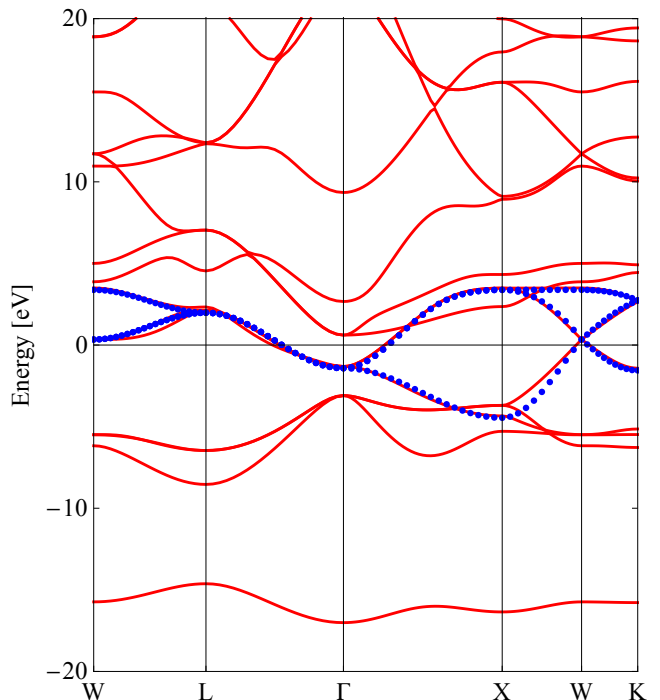


FIG. 2. The electron band dispersion of NbN obtained from the first-principles calculation (red curves) and that of the simplified model [Eq. (2), blue dots] with the hopping parameters fitted to the effective three-band model constructed from the maximally localized Wannier orbitals.

dispersion for the  $d_{xy}$  orbital is given by

$$\epsilon_{\mathbf{k},xy} = 4t \cos \frac{k_x}{2} \cos \frac{k_y}{2} + 2t'(\cos k_x + \cos k_y) + 4t'' \left( \cos \frac{k_y}{2} \cos \frac{k_z}{2} + \cos \frac{k_z}{2} \cos \frac{k_x}{2} \right). \quad (2)$$

The remaining band dispersions  $\epsilon_{\mathbf{k},yz}$  and  $\epsilon_{\mathbf{k},zx}$  are given by permuting  $x$ ,  $y$ , and  $z$  in  $\epsilon_{\mathbf{k},xy}$ . The three hopping parameters  $t$ ,  $t'$ , and  $t''$  are fitted with the three bands constructed from the maximally localized Wannier orbitals. The results are  $t = -0.79$  eV,  $t' = -0.22$  eV, and  $t'' = 0.19$  eV, which slightly deviate from the previous result in Ref. [18]. The difference arises because the previous study fit the expression (2) directly with the original band structures (corresponding to red curves in Fig. 2), while here we fit Eq. (2) using the band dispersion of the maximally localized Wannier orbitals.

In Fig. 2, we show the simplified band dispersions  $\epsilon_{\mathbf{k}n}$  by blue dots. One can see that both of the band dispersions constructed from the density functional calculation and from the simplified model (2) agree fairly well with each other. We employ the simplified dispersion  $\epsilon_{\mathbf{k}n}$  for the model-based calculation of THG in Sec. IV, where we need higher-order derivatives of the dispersion such as  $\frac{\partial^2 \epsilon_{\mathbf{k}n}}{\partial k_i \partial k_j}$  that can be analytically evaluated with the ex-

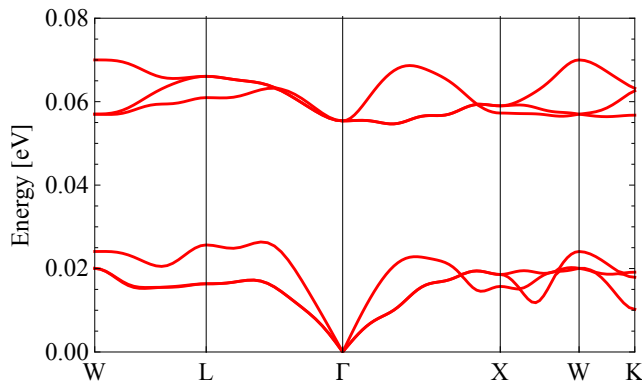


FIG. 3. The phonon dispersion of NbN obtained from the first principles calculation.

pression (2).

The effective model for phonons is represented by the Hamiltonian,

$$H_{\text{ph}} = \sum_{\mathbf{q}\nu} \omega_{\mathbf{q}\nu} b_{\mathbf{q}\nu}^\dagger b_{\mathbf{q}\nu}, \quad (3)$$

where  $\omega_{\mathbf{q}\nu}$  is the phonon frequency, and  $b_{\mathbf{q}\nu}^\dagger$  is the creation operator of phonons with momentum  $\mathbf{q}$  at  $\nu$ th branch. There are six phonon modes ( $\nu = 1, \dots, 6$ ) in total, corresponding to two atoms (Nb and N) in the unit cell each of which can oscillate along three orthogonal directions ( $x$ ,  $y$ , and  $z$ ). In Fig. 3, we plot the phonon band dispersion  $\omega_{\mathbf{q}\nu}$  of NbN obtained from the first principles calculation. Three of them are acoustic phonons with linear dispersions around  $\Gamma$  point, while the rest are optical phonons with energy gaps. Here we do not see imaginary phonon frequencies, implying that the present lattice structure is dynamically stable.

The electron-phonon coupling term is written as

$$H_{\text{el-ph}} = \frac{1}{\sqrt{N_{\mathbf{q}}}} \sum_{\mathbf{k}\mathbf{q}} \sum_{m\nu\sigma} g_{m\nu}^\nu(\mathbf{k}, \mathbf{q}) c_{\mathbf{k}+\mathbf{q}m\sigma}^\dagger c_{\mathbf{k}n\sigma} \times (b_{\mathbf{q}\nu} + b_{-\mathbf{q}\nu}^\dagger), \quad (4)$$

where  $m, n = xy, yz, zx$ , and  $g_{m\nu}^\nu(\mathbf{k}, \mathbf{q})$  represents the matrix elements of the multiband electron-phonon coupling constant estimated from the density function perturbation theory. The calculations of the matrix elements are done in the maximally localized Wannier orbital basis [47]<sup>1</sup>.

The electron-phonon coupling mediates an effective attraction between the electrons,  $-V_{mn}(\mathbf{k}, \mathbf{q}, \omega) = \sum_{\nu} |g_{m\nu}^\nu(\mathbf{k}, \mathbf{q})|^2 D_{\mathbf{q}\nu}^{\text{ph}}(\omega)$ , where we factor out the minus

sign in front of  $V_{mn}$  to indicate the attractive interaction, and  $D_{\mathbf{q}\nu}^{\text{ph}}(\omega) = 2\omega_{\mathbf{q}\nu}/(\omega^2 - \omega_{\mathbf{q}\nu}^2)$  is the phonon propagator. If we neglect the retardation effect of the phonon-mediated attraction and take the static part ( $\omega = 0$ ), the phonon-mediated attraction is given by  $V_{mn}(\mathbf{k}, \mathbf{q}) = \sum_{\nu} |g_{m\nu}^\nu(\mathbf{k}, \mathbf{q})|^2 \frac{2}{\omega_{\mathbf{q}\nu}}$ . By taking the momentum average of the attraction, we obtain the following BCS-type Hamiltonian:

$$H_{\text{el-el}} = -\frac{1}{N_{\mathbf{k}}} \sum_{\mathbf{k}\mathbf{k}'mn} V_{mn} c_{\mathbf{k}m\uparrow}^\dagger c_{-\mathbf{k}m\downarrow}^\dagger c_{-\mathbf{k}'n\downarrow} c_{\mathbf{k}'n\uparrow}. \quad (5)$$

Here,  $V_{nn} \equiv V_{\text{intra}}$  and  $V_{mn} \equiv V_{\text{inter}}$  ( $m \neq n$ ) denote the averaged intraband and interband effective attractions, respectively. To estimate the realistic ratio between  $V_{\text{intra}}$  and  $V_{\text{inter}}$ , we compute the static part ( $\omega = 0$ ) of the Fermi-surface(FS)-averaged phonon-mediated attraction as

$$\langle V_{mn} \rangle_{\text{FS}} = \frac{1}{N_{\mathbf{q}} N_{\mathbf{k}}} \sum_{\mathbf{k}\mathbf{q}\nu} \frac{w_{\mathbf{k}+\mathbf{q}m} w_{\mathbf{k}n}}{D^2(\epsilon_F)} |g_{m\nu}^\nu(\mathbf{k}, \mathbf{q})|^2 \frac{2}{\omega_{\mathbf{q}\nu}}, \quad (6)$$

where  $D(\epsilon_F)$  is the density of states for each  $t_{2g}$  orbital at the Fermi energy (by symmetry, the density of states is the same among  $t_{2g}$  orbitals), and  $w_{\mathbf{k}n}$  is the weight of a maximally localized Wannier orbital  $n$  at the Fermi energy at momentum  $\mathbf{k}$  given by  $w_{\mathbf{k}n} = \sum_{\alpha} |U_{n\alpha}^{\mathbf{k}}|^2 \delta(\epsilon_{\alpha\mathbf{k}} - \epsilon_F)$ . Here,  $\alpha$  is the Kohn-Sham Bloch band index, and  $U_{n\alpha}^{\mathbf{k}}$  is the unitary matrix relating the Wannier and Bloch bases ( $c_{\mathbf{k}\alpha\sigma}^\dagger = \sum_n c_{\mathbf{k}n\sigma}^\dagger U_{n\alpha}^{\mathbf{k}}$ ). For the details of the derivation of Eq. (6), we refer to Appendix A. In practical numerical calculations,  $w_{\mathbf{k}n}$  is calculated using the Gaussian smearing  $e^{-x^2/2\eta^2}/\sqrt{2\pi}\eta$  with a broadening width  $\eta$ .

In Table I, we list the magnitude of the static part of the FS-averaged phonon-mediated attraction  $\langle V_{\text{intra}} \rangle_{\text{FS}}$  and  $\langle V_{\text{inter}} \rangle_{\text{FS}}$  for NbN. We note that the density of states  $D(\epsilon_F)$  is about 0.12 states/eV and that the coupling constant  $\lambda = D(\epsilon_F) (\langle V_{\text{intra}} \rangle_{\text{FS}} + 2 \langle V_{\text{inter}} \rangle_{\text{FS}})$  amounts to  $\sim 1$ , in accord with the previous estimates [33–36]. The important quantity in the following THG calculations is the ratio between the intraband and interband interactions  $V_{\text{inter}}/V_{\text{intra}}$  in Eq. (5). We find that the first-principles estimate of the ratio  $\langle V_{\text{inter}} \rangle_{\text{FS}} / \langle V_{\text{intra}} \rangle_{\text{FS}}$  is about 0.17-0.18. Referring to the *ab initio* value, in the following sections, we set the ratio  $V_{\text{inter}}/V_{\text{intra}}$  to be 0.18.

### III. METHOD FOR THE CALCULATION OF THIRD HARMONIC GENERATION

Having evaluated the effective intraband and interband pairing interactions for NbN evaluated in the previous section, we now move on to the calculation and classification of the THG susceptibility for NbN with impurities. Here the nonlinear susceptibilities are defined by

<sup>1</sup> Note that our tight-binding model in Eq. (1) is written in the Wannier basis. Since orbital-off-diagonal hoppings are negligible, the Wannier and band indices agree with each other.

TABLE I. The magnitude of the static part ( $\omega = 0$ ) of the Fermi-surface(FS)-averaged phonon-mediated attractions estimated from first principles for NbN. The column ‘‘Broadening’’ shows the broadening width  $\eta$  of the delta functions used to evaluate the FS average.  $V_{\text{intra}}$  and  $V_{\text{inter}}$  denote the intraband and interband attractions, respectively (see the text for details).

Broadening [Ry]	$\langle V_{\text{intra}} \rangle_{\text{FS}}$ [eV]	$\langle V_{\text{inter}} \rangle_{\text{FS}}$ [eV]	$\langle V_{\text{inter}} \rangle_{\text{FS}} / \langle V_{\text{intra}} \rangle_{\text{FS}}$
0.005	6.797	1.213	0.178
0.010	6.191	1.099	0.178
0.015	6.236	1.069	0.171
0.020	6.411	1.068	0.167
0.025	6.528	1.072	0.164
0.030	6.543	1.078	0.165
0.035	6.488	1.079	0.166
0.040	6.421	1.073	0.167
0.045	6.362	1.063	0.167
0.050	6.313	1.052	0.167

expanding the current with respect to the amplitude of the external field,

$$\mathbf{e} \cdot \mathbf{j}(t) = \chi_1 A(t) + \chi_2 A(t)^2 + \chi_3 A(t)^3 + \dots, \quad (7)$$

where  $\mathbf{e}$  is the polarization vector along which the current is measured, and  $A(t)$  is the amplitude of the vector potential. We are mostly concerned with the emitted light with  $\mathbf{e}$  parallel to the incident light. In parity symmetric systems (as is the case for NbN), the even-order terms are absent. The third coefficient  $\chi_3$  is the THG susceptibility that we are interested in. The induced current is accompanied by the electric polarization, which couples to electromagnetic fields and emits light. Thus, one can effectively regard the nonlinear susceptibilities as being proportional to the amplitude of the emitted light.

Our method of evaluating the THG susceptibility is based on the BCS mean-field approximation, where we neglect phonon retardation effects (see the discussion in Sec. I). We also do not explicitly consider dynamical screening effects due to long-range Coulomb interactions, which do not significantly modify the behavior of THG in superconductors [17]. For the treatment of impurities, we employ the self-consistent Born approximation, which is valid in the weak disorder case (i.e., the impurity scattering rate is much smaller than the hopping but can be larger than the superconducting gap). In the calculation of the THG susceptibility, we need to take into account the vertex corrections represented by impurity ladder diagrams [25, 27, 48].

### A. Formalism

Let us consider a multiband system described by the BCS Hamiltonian with the intraband and interband pair-

ing interactions and nonmagnetic impurity scatterings,

$$H_{\text{BCS}}(t) = \sum_{\mathbf{k}n\sigma} \epsilon_{\mathbf{k}-\mathbf{A}(t),n} c_{\mathbf{k}n\sigma}^\dagger c_{\mathbf{k}n\sigma} - \frac{1}{N_{\mathbf{k}}} \sum_{\mathbf{k}\mathbf{k}'mn} V_{mn} c_{\mathbf{k}m\uparrow}^\dagger c_{-\mathbf{k}m\downarrow}^\dagger c_{-\mathbf{k}'n\downarrow} c_{\mathbf{k}'n\uparrow} + \sum_{i\mathbf{m}n\sigma} v_{i\mathbf{m}n} (c_{i\mathbf{m}\sigma}^\dagger c_{i\mathbf{n}\sigma} + \text{h.c.}), \quad (8)$$

where  $\mathbf{A}(t)$  is the vector potential for external electromagnetic fields, and  $v_{i\mathbf{m}n}$  represents the impurity potential that hybridizes  $m$  and  $n$  bands at a lattice site  $i$ . We assume that  $v_{i\mathbf{m}n}$  is a Gaussian random variable with the disorder average given by  $\langle v_{i\mathbf{m}n} v_{i'\mathbf{m}'n'} \rangle_{\text{disorder}} = \gamma_{mn}^2 \delta_{ii'} \delta_{mm'} \delta_{nn'}$ . Here the impurity scattering rate is parametrized by the intraband and interband ones,  $\gamma_{\text{intra}} = \gamma_{nn}$  and  $\gamma_{\text{inter}} = \gamma_{mn}$  ( $m \neq n$ ), respectively.

To calculate real-frequency spectra, we introduce nonequilibrium (retarded, advanced, and lesser) Green’s functions for multiband superconductors,

$$G_{\mathbf{k}n,ab}^R(t, t') = -i\theta(t-t') \langle \{ \Psi_{\mathbf{k}n,a}(t), \Psi_{\mathbf{k}n,b}^\dagger(t') \} \rangle, \quad (9)$$

$$G_{\mathbf{k}n,ab}^A(t, t') = i\theta(t'-t) \langle \{ \Psi_{\mathbf{k}n,a}(t), \Psi_{\mathbf{k}n,b}^\dagger(t') \} \rangle, \quad (10)$$

$$G_{\mathbf{k}n,ab}^<(t, t') = i \langle \Psi_{\mathbf{k}n,b}^\dagger(t') \Psi_{\mathbf{k}n,a}(t) \rangle, \quad (11)$$

where  $\Psi_{\mathbf{k}n}^\dagger = (c_{\mathbf{k}n\uparrow}^\dagger \ c_{-\mathbf{k}n\downarrow})$  is the two-component Nambu spinor,  $a, b = 1, 2$  are the Nambu space indices, and  $\theta(t)$  is the step function [ $\theta(t) = 1$  ( $t \geq 0$ ) and  $\theta(t) = 0$  ( $t < 0$ )]. The Green’s functions satisfy the following Dyson equation,

$$[i\partial_t - \xi_{\mathbf{k}-\mathbf{A}(t)\hat{\tau}_3, n} \hat{\tau}_3] \hat{G}_{\mathbf{k}n}^\alpha(t, t') - \int d\bar{t} [\hat{\Sigma}_n(t, \bar{t}) \hat{G}_{\mathbf{k}n}^\alpha(\bar{t}, t')] = \delta^\alpha(t, t') \quad (\alpha = R, A, <), \quad (12)$$

where  $\xi_{\mathbf{k},n} = \epsilon_{\mathbf{k},n} - \mu$  ( $\mu$  is the chemical potential),  $\hat{\tau}_i$  ( $i = 1, 2, 3$ ) are Pauli matrices in the Nambu space,



and  $\hat{\Sigma}_n(t, t')$  is the self-energy. We put a hat on a matrix which has Nambu spinor indices. The superscript  $\alpha$  should be understood according to the Langreth rule [49], i.e.,  $(XY)^R = X^R Y^R$ ,  $(XY)^A = X^A Y^A$ ,  $(XY)^< = X^R Y^< + X^< Y^A$ , and so on. We use a convention of  $\delta^R(t, t') = \delta^A(t, t') = \delta(t, t')$  (Dirac's delta function) and  $\delta^<(t, t') = 0$ . In equilibrium with  $\mathbf{A} = 0$ , the retarded Green's function is given in a Fourier transformed form as

$$\hat{G}_{kn}^R(\omega) = \left[ (\omega + i\epsilon)\hat{\tau}_0 - \xi_{kn}\hat{\tau}_3 - \hat{\Sigma}_n^R(\omega) \right]^{-1}, \quad (13)$$

where  $\epsilon$  is a positive infinitesimal constant and  $\hat{\tau}_0$  represents the unit matrix. In equilibrium, the advanced and lesser Green's functions are given by  $\hat{G}_{kn}^A(\omega) = \hat{G}_{kn}^R(\omega)^\dagger$  and  $\hat{G}_{kn}^<(\omega) = f(\omega)[\hat{G}_{kn}^A(\omega) - \hat{G}_{kn}^R(\omega)]$ , where  $f(\omega) = 1/(e^{\beta\omega} + 1)$  is the Fermi distribution function and  $\beta = (k_B T)^{-1}$  is the inverse temperature.

In the BCS and self-consistent Born approximations, the self-energy is determined by

$$\hat{\Sigma}_n^\alpha(t, t') = \Delta_n(t)\hat{\tau}_1\delta^\alpha(t, t') + \sum_m \gamma_{nm}^2 \frac{1}{N_{\mathbf{k}}} \sum_{\mathbf{k}} \hat{\tau}_3 \hat{G}_{km}^\alpha(t, t') \hat{\tau}_3, \quad (14)$$

where  $\Delta_n$  is the superconducting gap for a band  $n$  defined by

$$\Delta_n(t) = \frac{i}{2} \sum_m V_{nm} \frac{1}{N_{\mathbf{k}}} \sum_{\mathbf{k}} \text{Tr}[\hat{\tau}_1 \hat{G}_{km}^<(t, t)]. \quad (15)$$

In the above, we have assumed that Cooper pairs are formed within each band. The equilibrium superconducting gap, self-energy, and Green's functions are self-consistently determined by Eqs. (12), (14), and (15). In Fig. 4, we show the diagrammatic representation for the Dyson equation in the BCS mean-field and self-consistent Born approximations.

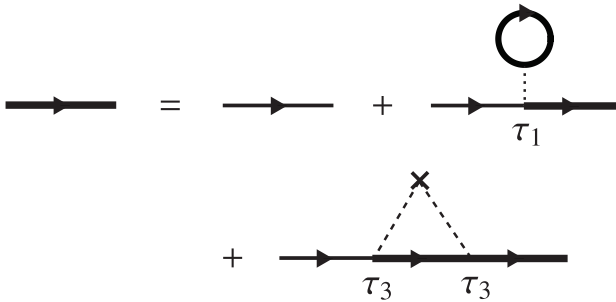


FIG. 4. The Dyson equation for the electron Green's function in the BCS mean-field and self-consistent Born approximations. The thin and bold lines represent the noninteracting and interacting Green's functions, respectively. The dotted line represents the pairing interaction, and the dashed lines represent the impurity scattering.

In order to evaluate the third harmonic generation, we employ the field-derivative approach developed in

Ref. [23], which allows one to systematically derive nonlinear optical susceptibilities. The idea is to analytically differentiate the current,

$$\mathbf{j}(t) = -\frac{i}{N_{\mathbf{k}}} \sum_{kn} \text{Tr}(\mathbf{v}_{\mathbf{k}-\mathbf{A}(t)\hat{\tau}_3, n} \hat{G}_{kn}^<(t, t)), \quad (16)$$

with respect to the amplitude of the external field  $\mathbf{A}(t) = \mathbf{e}Ae^{-i\Omega t}$ , where  $\mathbf{v}_{\mathbf{k}, n} = \frac{\partial \epsilon_{\mathbf{k}n}}{\partial \mathbf{k}}$  is the group velocity,  $\mathbf{e}$  is the unit polarization vector ( $\|\mathbf{e}\| = 1$ ),  $A$  and  $\Omega$  are the amplitude and frequency of the field. In this process, we repeatedly differentiate the self-consistent equations (12), (14), and (15) in the presence of the external field  $\mathbf{A}(t)$ .

Since odd-order derivatives of the self-energy  $\hat{\Sigma}_n$  and the superconducting gap  $\Delta_n$  vanish due to the parity symmetry of the system, what we need to calculate for the THG susceptibility is the second derivatives,  $\ddot{\Sigma}_n(\omega) = \frac{\partial^2}{\partial A^2} \hat{\Sigma}_n(\omega)$  and  $\ddot{\Delta}_n = \frac{\partial^2}{\partial A^2} \Delta_n$  [23] (the derivative with respect to  $A$  is denoted by dots), which are self-consistently determined by the doubly differentiated equations. By taking the second derivative of Eq. (12), one obtains the relation

$$\begin{aligned} \ddot{G}_{kn}^\alpha(\omega) &= [\hat{G}_{kn}(\omega + 2\Omega)\dot{\epsilon}_{kn}\hat{\tau}_3\hat{G}_{kn}(\omega)]^\alpha \\ &+ 2[\hat{G}_{kn}(\omega + 2\Omega)\dot{\epsilon}_{kn}\hat{G}_{kn}(\omega + \Omega)\dot{\epsilon}_{kn}\hat{G}_{kn}(\omega)]^\alpha \\ &+ [\hat{G}_{kn}(\omega + 2\Omega)\ddot{\Sigma}_n(\omega)\hat{G}_{kn}(\omega)]^\alpha \end{aligned} \quad (17)$$

with  $\alpha = R, A, <$ . In Eq. (17), one can see that there are two types of couplings to the light field: one is the diamagnetic coupling ( $\propto \rho \mathbf{A}^2$ ;  $\rho$  is the electron density) given through  $\dot{\epsilon}_{\mathbf{k}}$ , and the other is the paramagnetic coupling ( $\propto \mathbf{j} \cdot \mathbf{A}$ ) given through two  $\dot{\epsilon}_{\mathbf{k}}$ 's. The role of the latter paramagnetic coupling has been emphasized as a dominant interaction between the Higgs mode and electromagnetic fields [23].

The second derivative of the self-energy  $\ddot{\Sigma}_n(\omega)$  is determined by doubly differentiating Eq. (14),

$$\ddot{\Sigma}_n^\alpha(\omega) = \ddot{\Delta}_n \hat{\tau}_1^\alpha + \sum_m \gamma_{nm}^2 \frac{1}{N_{\mathbf{k}}} \sum_{\mathbf{k}} \hat{\tau}_3 \ddot{G}_{km}^\alpha(\omega) \hat{\tau}_3, \quad (18)$$

where  $\tau_1^\alpha = \tau_1$  for  $\alpha = R, A$  and  $\tau_1^\alpha = 0$  for  $\alpha = <$ . The first term on the right hand side of Eq. (18) represents the effect of amplitude fluctuation of the superconducting gap (i.e., the Higgs mode), while the second term corresponds to the impurity-ladder vertex corrections. Finally, the second derivative of the superconducting gap  $\ddot{\Delta}_n$  is given by doubly differentiating Eq. (15),

$$\ddot{\Delta}_n = \frac{i}{2} \sum_m V_{nm} \frac{1}{N_{\mathbf{k}}} \sum_{\mathbf{k}} \int \frac{d\omega}{2\pi} \text{Tr}[\hat{\tau}_1 \ddot{G}_{km}^<(\omega)]. \quad (19)$$

The second derivatives,  $\ddot{G}_{kn}(\omega)$ ,  $\ddot{\Sigma}_n(\omega)$ , and  $\ddot{\Delta}_n$ , are calculated by solving the self-consistent equations (17), (18), and (19). The results are plugged into the third

TABLE II. Classification of the THG susceptibility according to the physical origin (quasiparticle or Higgs mode), the coupling channel to light (diamagnetic or paramagnetic), and the diagrammatic representation in the presence of impurities. In the diagrams, the lines with arrows, single wavy lines, double wavy lines, and shaded squares represent the electron propagators, photon propagators, Higgs-mode propagators, and impurity ladder corrections, respectively. In each diagram, three of the four photon propagators carry incoming frequencies  $\Omega$ , while the rest carries outgoing frequency  $3\Omega$ . The fifth column shows whether each THG susceptibility has a resonance at frequency  $2\Omega = 2\Delta$ . The sixth column shows whether each THG susceptibility is robust against nonmagnetic impurities.

susceptibility	origin	channel	diagram	resonance at $2\Omega = 2\Delta$	impurity robustness
$\chi_{\text{qp}}^{(1)}$	quasiparticle	diamagnetic			✓
$\chi_{\text{qp}}^{(2)}$	quasiparticle	paramagnetic			
$\chi_{\text{qp}}^{(3)}$	quasiparticle	diamagnetic		✓	✓
$\chi_{\text{qp}}^{(4)}$	quasiparticle	mixed		✓	
$\chi_{\text{qp}}^{(5)}$	quasiparticle	paramagnetic		✓	
$\chi_{\text{H}}^{(1)}$	Higgs mode	diamagnetic		✓	✓
$\chi_{\text{H}}^{(2)}$	Higgs mode	mixed		✓	
$\chi_{\text{H}}^{(3)}$	Higgs mode	paramagnetic		✓	

derivative of the current  $\ddot{\mathbf{j}}$  to obtain the THG susceptibility. In this paper, we focus on the THG induced along the polarization direction of the incident light. More details of the derivation of the THG susceptibility are described in Appendix B.

## B. Classification of THG susceptibilities

In Table II, we list all the THG diagrams including both the quasiparticle and Higgs-mode contributions. The distinction between the two contributions is defined by whether or not the diagram includes the Higgs-mode propagator depicted by the double wavy lines. The Higgs-mode propagator contains the fluctuation of the superconducting gap amplitude, which is diagrammatically shown in Fig. 5. Here the dotted lines represent

the bare attractive interaction  $V_{mn}$ , while the bold lines with arrows represent the electron propagator  $\hat{G}_{kn}$ . The shaded square represents the impurity-ladder correction, as shown in Fig. 6.

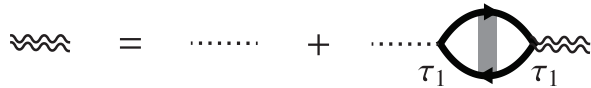


FIG. 5. The self-consistent equation for the Higgs-mode propagator (double wavy lines).

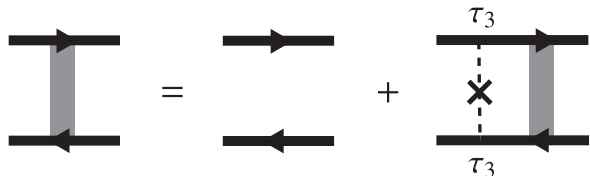


FIG. 6. The self-consistent equation for the impurity ladder correction (shaded squares).

There are five topologically inequivalent diagrams for quasiparticles and three diagrams for the Higgs mode. They have different couplings to external laser fields (single wavy lines) classified into the paramagnetic, diamagnetic, and mixed channels in Table II. Each outer vertex attached to  $\ell$  photon lines in the THG diagram is assigned to the  $\ell$ th derivative  $\frac{d^\ell \epsilon_k}{dA^\ell}$ , which has the same parity as the density if  $\ell$  is even and has the same parity as the current if  $\ell$  is odd. Hence we call the channel of the coupling to light diamagnetic when  $\ell$  is even and paramagnetic when  $\ell$  is odd. There are THG diagrams in which the paramagnetic and diamagnetic couplings coexist, which we refer to as the mixed channel. We remark that the impurity correction is absent for vertices with odd number of photon lines since odd parity terms vanish after momentum summation.

In Table II, we also show which THG susceptibility has a resonance at frequency  $2\Delta$ . As we will see in Sec. IV,  $\chi_{\text{qp}}^{(i)}$  ( $i = 3, 4, 5$ ) and  $\chi_{\text{H}}^{(i)}$  ( $i = 1, 2, 3$ ) generally show the resonance. The resonance of  $\chi_{\text{H}}^{(i)}$  originates from the collective Higgs mode whose energy gap corresponds to  $2\Delta$ . On the other hand, the quasiparticle contributions  $\chi_{\text{qp}}^{(i)}$  also exhibit the resonance at  $2\Delta$ , which is equal to the lowest pair-breaking energy. The degeneracy of the resonance energy between the Higgs mode and quasiparticles forces us to distinguish them by properties other than the resonance frequency, as discussed in Sec. I.

We also indicate in Table II which THG susceptibility is robust (insensitive) against nonmagnetic impurity scattering. Generally the THG susceptibility in the diamagnetic coupling channels do not depend on the impurity scattering rate, while the paramagnetic and mixed channels exhibit strong impurity dependence, which plays a

key role in enhancing the Higgs-mode contribution in THG in dirty regimes. This fact is related to Anderson's theorem [50] (which states robustness of the superconducting gap against nonmagnetic impurity scattering in equilibrium  $s$ -wave superconductors), which can be generalized to robustness of the Higgs mode [25, 51]. We confirm the robustness of each THG channel against impurity scattering by numerical simulations in Sec. IV.

#### IV. THIRD HARMONIC GENERATION IN NbN SUPERCONDUCTOR

Based on the method described in Sec. III, we numerically evaluate the THG susceptibilities for NbN superconductors. We use the simplified band dispersion of NbN (2) derived from the first principles calculation in Sec. II. Throughout this section, we use eV as the unit of energy, and fix the ratio between the intraband and interband phonon-mediated interactions to be  $V_{\text{inter}}/V_{\text{intra}} = 0.18$  (Sec. II). The absolute value of the interaction is chosen such that the superconducting gap is fixed. For the numerical feasibility, we take a relatively large superconducting gap  $2\Delta = 0.8$  to maintain sufficiently high frequency and momentum resolution (cf. the real gap size is in the order of few meV). This requires us to take  $50 \times 50 \times 50 = 125000$   $k$ -points. We have checked that the results do not change qualitatively as we vary the value of  $2\Delta$  within our reach of numerical calculations. The intraband and interband impurity scattering rates  $\gamma_{\text{intra}}$  and  $\gamma_{\text{inter}}$  are free parameters. In order for the self-consistent Born approximation to be valid (which is the case in the experimental situation [16, 18]), the impurity scattering rates should be sufficiently smaller than the Fermi energy ( $\gamma_{\text{intra}}, \gamma_{\text{inter}} \ll \epsilon_F$ ). Here we restrict ourselves to  $\gamma_{\text{intra}}/2\Delta, \gamma_{\text{inter}}/2\Delta \leq 2.5$  (cf.  $\epsilon_F \sim 3 - 4$ ). We first focus on the case of  $\gamma_{\text{intra}} = 2\gamma_{\text{inter}} = \gamma$  with  $0 \leq \gamma/2\Delta \leq 2.5$ . Then we scan the parameter space of  $(\gamma_{\text{intra}}, \gamma_{\text{inter}})$  with  $0 \leq \gamma_{\text{intra}}/2\Delta, \gamma_{\text{inter}}/2\Delta \leq 2.5$ . We set the filling to be one third for NbN superconductor (two electrons in the three bands) and the inverse temperature  $\beta = 50$ , which is sufficiently lower than the superconducting critical temperature. In the numerical simulation, we take a finite value of the constant  $\epsilon = 0.01$  [which has been introduced as a positive infinitesimal in Eq. (13)].

##### A. Channel-resolved THG intensity

We first present the results for the THG intensity in NbN superconductors in the channel resolved manner as classified in Table II in Sec. III. In this subsection, the polarization direction  $e$  of light is set to be parallel to  $x$  crystal axis.

In Fig. 7, we plot the frequency dependence of the THG intensity for NbN superconductors with  $\gamma_{\text{intra}}/2\Delta = 2.0$  and  $\gamma_{\text{inter}}/2\Delta = 1.0$  (the dirty regime) in the linear [Fig. 7(a)] and log scale [Fig. 7(b)]. The leading con-



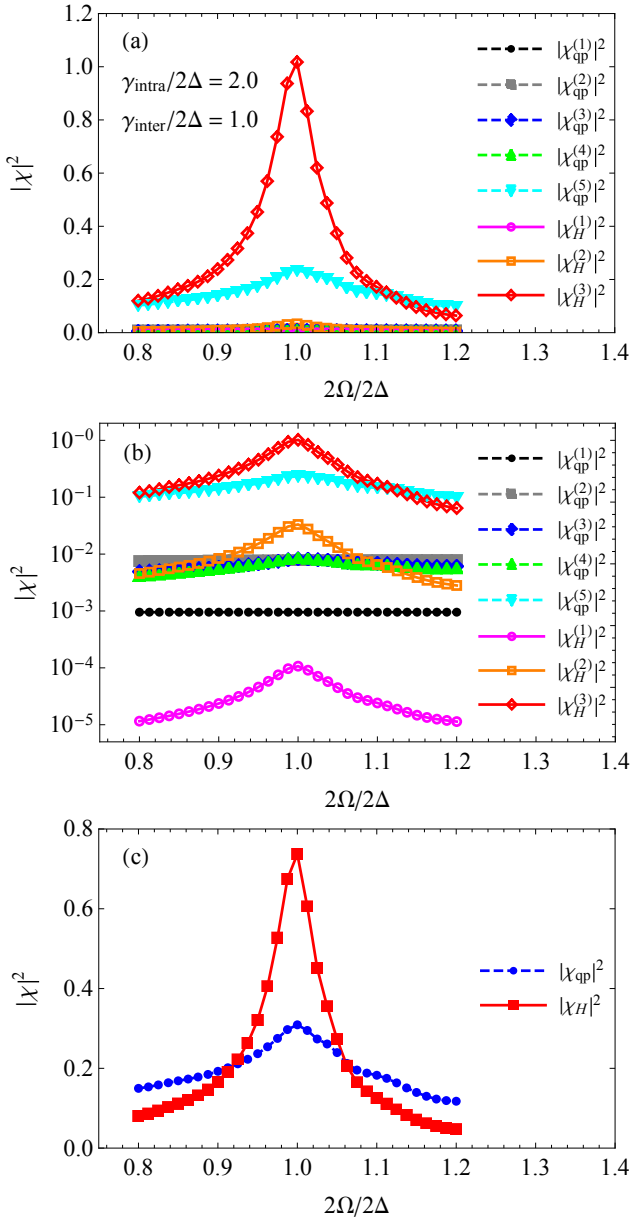


FIG. 7. (a), (b) Channel-resolved THG intensity for NbN superconductors with  $\gamma_{\text{intra}}/2\Delta = 2.0$  and  $\gamma_{\text{inter}}/2\Delta = 1.0$  as a function of the frequency  $2\Omega/2\Delta$  in the linear (a) and log scale (b). (c) The total quasiparticle and Higgs-mode contributions to the THG intensity for the model of NbN superconductors (8). The polarization of light is parallel to  $x$  crystal axis ( $\theta = 0^\circ$ ).

tribution comes from the Higgs mode in the paramagnetic channel ( $\chi_{\text{H}}^{(3)}$ ), showing a clear resonance peak at  $2\Omega = 2\Delta$ . The second dominant contribution comes from quasiparticles in the paramagnetic channel ( $\chi_{\text{qp}}^{(5)}$ ), which has a relatively broadened resonance peak at  $2\Omega = 2\Delta$ . One can see that the resonance at  $2\Omega = 2\Delta$  occurs in the channels  $\chi_{\text{qp}}^{(i)}$  ( $i = 3, 4, 5$ ) and  $\chi_{\text{H}}^{(i)}$  ( $i = 1, 2, 3$ ), being consistent with Table II. In Fig. 7(c), we plot the to-

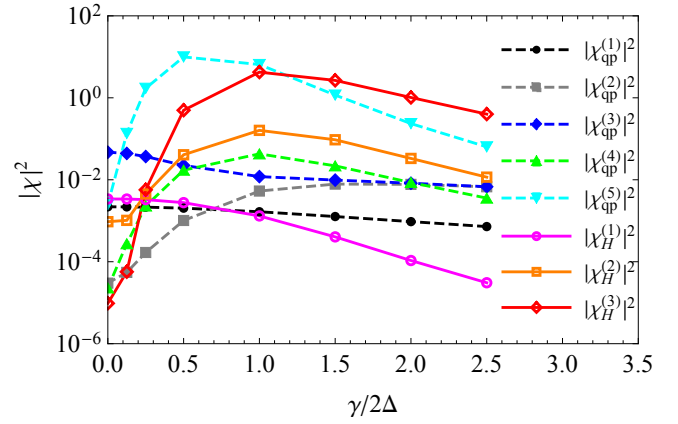


FIG. 8. Channel-resolved THG intensity for the model of NbN superconductors (8) at frequency  $2\Omega = 2\Delta$  as a function of the impurity scattering rate  $\gamma_{\text{intra}} = 2\gamma_{\text{inter}} = \gamma$ . The polarization of light is parallel to  $x$  crystal axis ( $\theta = 0^\circ$ ). The vertical axis is in the log scale.

tal quasiparticle ( $|\chi_{\text{qp}}|^2 = |\sum_{i=1}^5 \chi_{\text{qp}}^{(i)}|^2$ ) and Higgs-mode ( $|\chi_{\text{H}}|^2 = |\sum_{i=1}^3 \chi_{\text{H}}^{(i)}|^2$ ) contributions to the THG intensity in the dirty regime of NbN superconductors. Clearly, the Higgs-mode contribution is larger than the quasiparticles. This result agrees with the previous observations that the Higgs-mode contribution is drastically enhanced due to impurity scattering [25–27]. Similar enhancement has been found due to phonon retardation effects [23].

In Fig. 8, we plot the impurity dependence of the THG intensity for NbN superconductors at frequency  $2\Omega = 2\Delta$ , where we set  $\gamma_{\text{intra}} = 2\gamma_{\text{inter}} = \gamma$ . The THG intensity in the paramagnetic and mixed channels [ $|\chi_{\text{qp}}^{(i)}|^2$  ( $i = 2, 4, 5$ ) and  $|\chi_{\text{H}}^{(i)}|^2$  ( $i = 2, 3$ )] show sensitive dependence on  $\gamma$ , while those in the diamagnetic channel [ $|\chi_{\text{qp}}^{(i)}|^2$  ( $i = 1, 3$ ) and  $|\chi_{\text{H}}^{(1)}|^2$ ] is less sensitive (especially at small  $\gamma/2\Delta$ ). This observation supports the general behavior of the THG susceptibility against impurities shown in Table II in Sec. III. The  $\gamma$  dependence of the quasiparticle and Higgs-mode contributions in the diamagnetic and paramagnetic channels is qualitatively consistent with the previous order estimate in [26].

In the clean limit ( $\gamma \rightarrow 0$ ), the most dominant contribution comes from quasiparticles in the diamagnetic channel ( $\chi_{\text{qp}}^{(3)}$ ). The second dominant one is the Higgs-mode contribution in the diamagnetic channel ( $\chi_{\text{H}}^{(1)}$ ). The paramagnetic channel is also present at  $\gamma = 0$ , since we broaden the THG spectrum by taking the finite value of  $\epsilon$  (so that the results at  $\gamma = 0$  slightly deviate from the ideal clean limit). As we increase  $\gamma$ , the quasiparticle contribution in the paramagnetic channel ( $\chi_{\text{qp}}^{(5)}$ ) quickly grows, and exceeds over the other components. At the same time, the Higgs-mode contribution in the paramagnetic channel ( $\chi_{\text{H}}^{(3)}$ ) also grows rapidly. Up to  $\gamma/2\Delta \lesssim 1$ ,  $\chi_{\text{qp}}^{(5)}$  remains to be most dominant. When the system enters the dirty regime ( $\gamma/2\Delta \gtrsim 1$ ), the Higgs mode takes

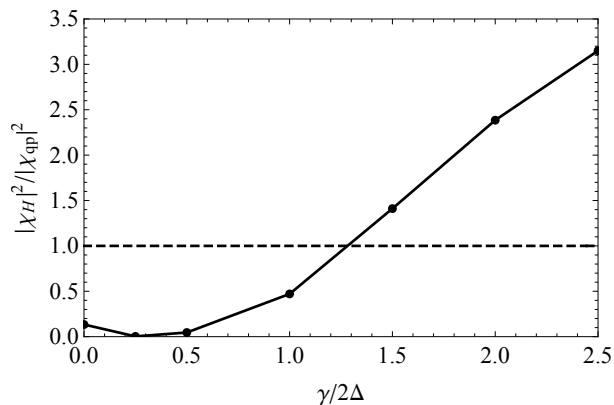


FIG. 9. The ratio  $|\chi_H|^2/|\chi_{qp}|^2$  between the Higgs-mode and quasiparticle contributions to the THG intensity for the model of NbN superconductors (8) as a function of the impurity scattering rate  $\gamma_{\text{intra}} = 2\gamma_{\text{inter}} = \gamma$  at frequency  $2\Omega = 2\Delta$ . The polarization of light is parallel to  $x$  crystal axis ( $\theta = 0^\circ$ ).

over the dominant part of the THG resonance, and  $\chi_H^{(3)}$  becomes the largest contribution. This tendency seems to continue toward the dirty limit. The maximum magnitude of the THG intensity in the paramagnetic channel is attained around  $\gamma \sim \Delta$ , in agreement with the previous results [26].

In Fig. 9, we plot the ratio between the total Higgs-mode ( $|\chi_H|^2$ ) and quasiparticle ( $|\chi_{qp}|^2$ ) contributions to the THG intensity for NbN superconductors as a function of  $\gamma_{\text{intra}} = 2\gamma_{\text{inter}} = \gamma$ . In the clean regime ( $\gamma \lesssim 2\Delta$ ) the quasiparticle contribution is dominant, whereas in the dirty regime ( $\gamma \gtrsim 2\Delta$ ) the Higgs-mode contribution exceeds the quasiparticle one. We expect that the ratio  $|\chi_H|^2/|\chi_{qp}|^2$  continues to increase towards the dirty limit (as observed in the single-band case [27]), while our calculation is limited to  $\gamma/2\Delta \leq 2.5$  in order to maintain the validity of the self-consistent Born approximation. One can see a little increase of  $|\chi_H|^2/|\chi_{qp}|^2$  around  $\gamma/2\Delta = 0$ , which we attribute to the effect of the relatively large superconducting gap ( $2\Delta = 0.8$ ) and the finite broadening factor ( $\epsilon = 0.01$ ) in our simulation.

We separately change the intraband and interband impurity scattering rates to plot  $|\chi_H|^2/|\chi_{qp}|^2$  in Fig. 10. The quasiparticle dominant region is shown by blue in the color plot, while the Higgs dominant region is shown by red. The boundary between the two regions is roughly given by  $\gamma_{\text{intra}}/2\Delta \sim 1.75$  and  $\gamma_{\text{inter}}/2\Delta \sim 1$ . The interband scattering is more effective to enhance the Higgs-mode contribution than the intraband one, since the interband scattering takes place more frequently in three-band systems.

## B. Polarization-angle dependence

Next, we study the polarization-angle dependence of the THG intensity for NbN superconductors, which may

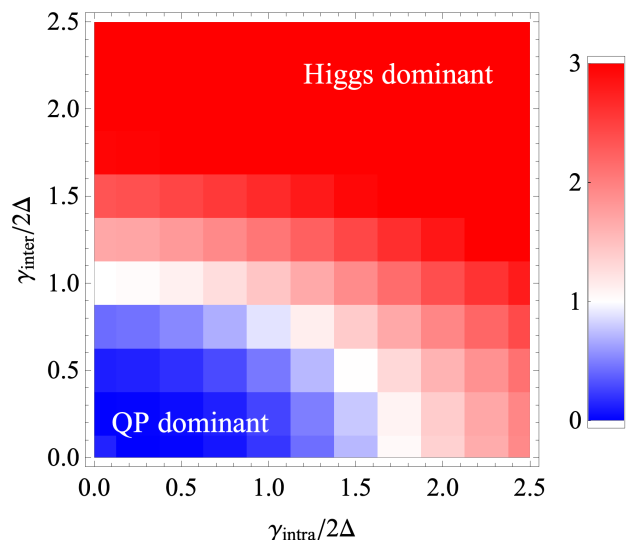


FIG. 10. The ratio  $|\chi_H|^2/|\chi_{qp}|^2$  between the Higgs-mode and quasiparticle (QP) contributions to the THG intensity for the model of NbN superconductors (8) at frequency  $2\Omega = 2\Delta$  plotted in the space of  $\gamma_{\text{intra}}/2\Delta$  and  $\gamma_{\text{inter}}/2\Delta$ . The polarization of light is parallel to  $x$  crystal axis ( $\theta = 0^\circ$ ).

allow one to distinguish the quasiparticle and Higgs-mode contributions in experiments. The polarization angle is measured from the  $x$  crystal axis, and the polarization vector  $e$  is rotated in the  $xy$  plane.

In Fig. 11, we plot the normalized  $|\chi_{qp}(\theta)|^2/|\chi_{qp}(\theta = 0^\circ)|^2$  and  $|\chi_H(\theta)|^2/|\chi_H(\theta = 0^\circ)|^2$  for several values of  $\gamma_{\text{intra}}/2\Delta$  and  $\gamma_{\text{inter}}/2\Delta$ . In the clean limit [Fig. 11(a)], we find that the quasiparticle contribution grows monotonically by  $\sim 6\%$  as the angle varies from  $\theta = 0^\circ$  to  $45^\circ$ , whereas the Higgs-mode contribution decreases by  $\sim 7\%$ . The angle dependence of quasiparticles arises due to the anisotropic band structure of NbN. The change of the quasiparticle contribution from  $\theta = 0^\circ$  to  $45^\circ$  is smaller than that of the previous result [18]. This is mainly due to the difference of the hopping parameters that we used in the effective model of NbN. The angle dependence of the Higgs mode in the clean limit with small  $V_{\text{inter}}/V_{\text{intra}}$  is consistent with the previous study [28].

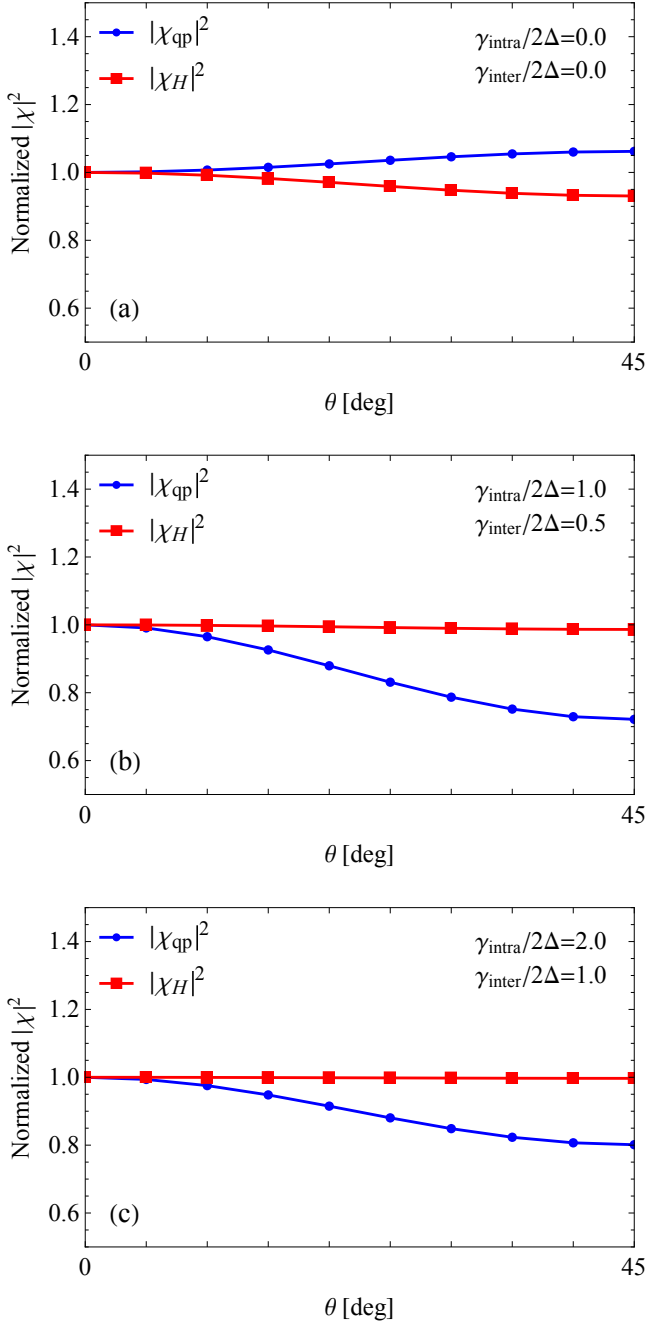


FIG. 11. The polarization-angle dependence of the quasiparticle and Higgs-mode contributions to the THG intensity for the model of NbN superconductors (8) at frequency  $2\Omega = 2\Delta$  with (a)  $\gamma_{intra}/2\Delta = 0.0$ ,  $\gamma_{inter}/2\Delta = 0.0$ , (b)  $\gamma_{intra}/2\Delta = 1.0$ ,  $\gamma_{inter}/2\Delta = 0.5$ , and (c)  $\gamma_{intra}/2\Delta = 2.0$ ,  $\gamma_{inter}/2\Delta = 1.0$ . Each quasiparticle and Higgs-mode contribution is normalized by the value at  $\theta = 0^\circ$ , respectively.

As we increase  $\gamma_{intra} = 2\gamma_{inter} = \gamma$  [Fig. 11(b),(c)], we observe qualitatively different polarization-angle dependence for quasiparticles. Namely,  $|\chi_{qp}|^2$  decreases by  $\sim 20 - 30\%$  as  $\theta$  changes from  $0^\circ$  to  $45^\circ$ . This behavior is mostly coming from the paramagnetic channel, which be-

comes dominant in the dirty regime. Namely, the quasiparticle contribution in the paramagnetic channel always tends to decrease from  $\theta = 0^\circ$  to  $45^\circ$  for arbitrary impurity scattering rates. The transition from the increasing to decreasing dependence on the polarization angle is very rapid, taking place around  $\gamma/2\Delta \sim 0.1$  where the paramagnetic channel starts to exceed the diamagnetic one. Contrary to the significant angle dependence for quasiparticles, the Higgs-mode contribution quickly becomes isotropic as one deviates from the clean limit. The angle dependence of the Higgs-mode contribution is no larger than 1.5% at  $\gamma/2\Delta \geq 1$ .

In Fig. 12, we plot  $|\chi_{qp}(\theta = 45^\circ)|^2/|\chi_{qp}(\theta = 0^\circ)|^2$  [Fig. 12(a)] and  $|\chi_H(\theta = 45^\circ)|^2/|\chi_H(\theta = 0^\circ)|^2$  [Fig. 12(b)] in the space of  $\gamma_{intra}/2\Delta$  and  $\gamma_{inter}/2\Delta$ . The quasiparticle contribution generally shows clear angle dependence for arbitrary impurity scattering rates. The increasing behavior of  $|\chi_{qp}|^2$  as a function of  $\theta$  is seen only in the vicinity of the clean limit, apart from which  $|\chi_{qp}|^2$  decreases by 5 – 50%. It seems that the angle dependence of the quasiparticle contribution does not vanish in the large intraband and/or interband impurity scattering limit. On the other hand, the angle dependence of the Higgs mode is suppressed for general impurity scattering rates as compared to quasiparticles. At the vanishing of the interband impurity scattering, the Higgs-mode contribution shows slight angle dependence of few %. One can also see that the angle dependence of both the quasiparticle and Higgs-mode contributions is sensitive to the interband impurity scattering rather than the intraband one in the dirty regime.

We expect that there are generally nonvanishing interband impurity scatterings in NbN. Then, one can use the polarization-angle dependence of THG to discriminate the Higgs-mode and quasiparticle contributions in the dirty regime of multiband superconductors. The optical conductivity measurement [16, 18] suggests that the NbN samples used in the THG experiment is close to the dirty limit ( $\gamma/2\Delta \gg 1$ ). The experimental observation of no angle dependence of THG in NbN superconductors [18] together with our results on the channel-resolved THG intensity in the dirty regime imply that the dominant contribution to the THG resonance originates from the Higgs mode.

Finally, let us comment on the behavior of the polarization-angle dependence on the ratio  $V_{inter}/V_{intra}$ . While we used the realistic value of  $V_{inter}/V_{intra} = 0.18$  for NbN estimated from first principles calculations throughout the paper, we have checked the angle dependence for several other values of  $V_{inter}/V_{intra}$  (not shown). In general, the angle dependence of the Higgs mode tends to be strongly suppressed as one increases  $V_{inter}/V_{intra}$  (for the case of  $V_{inter}/V_{intra} = 1$  in the clean limit, see [18]), whereas the angle dependence of quasiparticles remains almost unchanged. Although the realistic value of  $V_{inter}/V_{intra} = 0.18$  that we obtained in the present paper is not so large, we find that the Higgs-mode contribution is almost polarization-angle independent in the

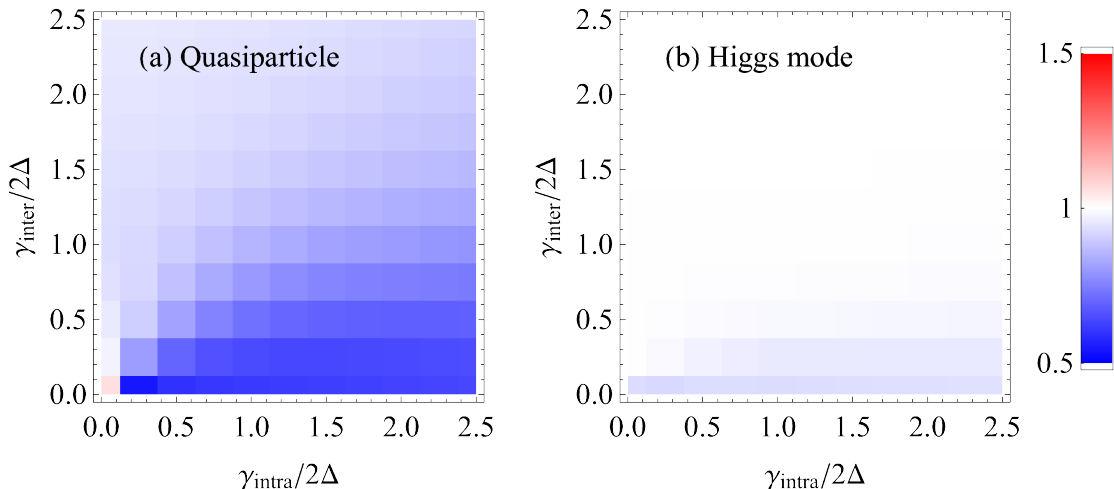


FIG. 12. The polarization-angle dependence of the quasiparticle (a) and Higgs-mode (b) contributions  $|\chi_{\text{qp,H}}(\theta = 45^\circ)|^2/|\chi_{\text{qp,H}}(\theta = 0^\circ)|^2$  to the THG intensity for the model of NbN superconductors (8) at frequency  $2\Omega = 2\Delta$  plotted in the space of the intraband and interband impurity scattering rates.

dirty regime for NbN superconductors. This suggests that the effect of impurity scattering plays an important role in understanding the behavior of the THG resonance in NbN superconductors.

## V. SUMMARY AND DISCUSSIONS

To summarize, we study the resonance of third harmonic generation and its polarization-angle dependence in disordered NbN superconductors based on the effective three-band model constructed from first principles calculations on the electron and phonon band structures of NbN. Using the density functional perturbation theory, we evaluate the band-resolved matrix elements of the electron-phonon coupling constants for NbN, and the ratio between the intraband and interband pairing interactions,  $V_{\text{inter}}/V_{\text{intra}}$ , is found to be about 0.17-0.18.

We input the evaluated ratio between the pairing interaction parameters in the effective model, whose THG susceptibility is calculated in the channel-resolved manner with the BCS mean-field and self-consistent Born approximations. The results show that in the dirty regime the dominant contribution to the THG resonance is given by the Higgs mode in the paramagnetic channel, which does not have polarization-angle dependence with nonvanishing interband impurity scattering. The second dominant one is given by quasiparticles in the paramagnetic channel, which exhibit clear polarization-angle dependence in the dirty regime. Our results are quite consistent with the polarization-resolved THG experiment on NbN superconductors [18], which have found no polarization-angle dependence in the THG resonance. It will be interesting if one can test the impurity dependence of the THG by controlling impurity concentration in NbN in future experiments.

While we have focused on Higgs amplitude mode in the present paper, there could arise the collective phase mode coupled to electromagnetic fields at low energies in disordered superconductors [4, 52, 53]. Since (i) the mode energy is generally different from  $2\Delta$ , (ii) it can exist only in the vicinity of  $T_c$ , and (iii) the phase mode is decoupled from the amplitude mode when an approximate particle-hole symmetry is present (as is the case in the BCS approximation), we expect that the phase mode (if it may exist) will not affect the THG resonance observed at frequency being half of  $2\Delta$ . In fact, such a phase mode has not been observed as the THG resonance in experiments. However, it would be worthwhile to pursue a possibility of detecting the low-energy phase mode by nonlinear optical responses in the future.

Our scheme of classifying and calculating THG susceptibilities for disordered superconductors from first principles can be applied not only to NbN but also to other superconductors. Interesting future applications include the THG resonance in  $\text{MgB}_2$ , a multigap superconductor with multiple Higgs modes as well as the Leggett mode [54–57], and  $\text{NbSe}_2$ , where superconductivity and charge density wave coexist. For unconventional superconductors such as cuprates [58–63] and iron-based superconductors, we need to extend the present formalism to take into account strong correlation effects beyond the BCS approximation in THG, which we leave as a future problem.

## ACKNOWLEDGMENTS

We acknowledge R. Shimano and Y. Murotani for valuable discussions. We thank various discussions at the international conference of Ultrafast and Nonlinear Dynamics of Quantum Materials (Paris Ultrafast 2019),

where part of the present work has been presented. N.T. acknowledges support by JSPS KAKENHI (Grants No. JP16K17729, No. JP20K03811) and JST PRESTO

(Grant No. JPMJPR16N7). Y.N. is supported by JSPS KAKENHI (Grants No. JP16H06345, No. JP17K14336 and No. JP18H01158).

### Appendix A: Derivation of Eq. (6)

In this appendix, we show the derivation of the Fermi-surface average of the effective phonon-mediated attractive interaction [Eq. (6) in the main text]. As we discussed in Sec. II, the momentum dependent effective interaction is given by  $V_{mn}(\mathbf{k}, \mathbf{q}) = \sum_{\nu} |g_{mn}^{\nu}(\mathbf{k}, \mathbf{q})|^2 \frac{2}{\omega_{q\nu}}$ . Here  $m$  and  $n$  ( $= xy, yz, zx$ ) represent the indices for maximally localized Wannier orbitals that we construct from the first principles band structure calculations. In the case of NbN, off-diagonal hopping matrix elements are negligibly small between different Wannier orbitals. If we neglect the off-diagonal components and if we appropriately choose the ordering of the orbital indices, the Fermi surface average of the effective interaction  $V_{mn}(\mathbf{k}, \mathbf{q})$  can be defined by

$$\langle V_{mn} \rangle_{\text{FS}} = \frac{\sum_{\mathbf{k}, \mathbf{q}} \delta(\epsilon_{\mathbf{k}+\mathbf{q}m} - \epsilon_F) \delta(\epsilon_{\mathbf{k}n} - \epsilon_F) V_{mn}(\mathbf{k}, \mathbf{q})}{\sum_{\mathbf{k}, \mathbf{q}} \delta(\epsilon_{\mathbf{k}+\mathbf{q}m} - \epsilon_F) \delta(\epsilon_{\mathbf{k}n} - \epsilon_F)} = \frac{1}{N_{\mathbf{k}} N_{\mathbf{q}}} \sum_{\mathbf{k}, \mathbf{q}} \frac{\delta(\epsilon_{\mathbf{k}+\mathbf{q}m} - \epsilon_F) \delta(\epsilon_{\mathbf{k}n} - \epsilon_F)}{D^2(\epsilon_F)} V_{mn}(\mathbf{k}, \mathbf{q}), \quad (\text{A1})$$

where the density of states at the Fermi energy for orbital  $n$  is given by

$$D(\epsilon_F) = \frac{1}{N_{\mathbf{k}}} \sum_{\mathbf{k}} \delta(\epsilon_{\mathbf{k}n} - \epsilon_F). \quad (\text{A2})$$

Note that the density of states  $D(\epsilon_F)$  does not depend on  $n$  due to the symmetry among the  $t_{2g}$  orbitals for NbN.

When off-diagonal hoppings in the Wannier basis are not negligible, Eq. (A1) is not directly applicable since the orbitals are highly mixed in the band basis near degenerate  $\mathbf{k}$  points. To see this, let us explicitly write the Hamiltonian in the Wannier basis,

$$H = \sum_{\mathbf{k}mn\sigma} c_{\mathbf{k}m\sigma}^{\dagger} H_{mn}^{\text{Wannier}}(\mathbf{k}) c_{\mathbf{k}n\sigma}, \quad (\text{A3})$$

with the diagonal elements  $H_{nn}^{\text{Wannier}}(\mathbf{k}) = \epsilon_{\mathbf{k}n}$ . If one goes to the band basis, the Hamiltonian becomes diagonal,

$$H = \sum_{\mathbf{k}\alpha\beta\sigma} c_{\mathbf{k}\alpha\sigma}^{\dagger} H_{\alpha\beta}^{\text{band}}(\mathbf{k}) c_{\mathbf{k}\beta\sigma}, \quad H_{\alpha\beta}^{\text{band}}(\mathbf{k}) = \epsilon_{\mathbf{k}\alpha} \delta_{\alpha\beta}, \quad (\text{A4})$$

where  $\alpha$  and  $\beta$  are the Bloch band indices.  $H^{\text{Wannier}}$  and  $H^{\text{band}}$  are related through a unitary transformation,

$$H_{mn}^{\text{Wannier}}(\mathbf{k}) = \sum_{\alpha\beta} U_{m\alpha}^{\mathbf{k}} H_{\alpha\beta}^{\text{band}}(\mathbf{k}) (U_{n\beta}^{\mathbf{k}})^*. \quad (\text{A5})$$

When there are off-diagonal hoppings between different orbitals, the level repulsion occurs and  $\epsilon_{\mathbf{k}\alpha}$  does not coincide with  $\epsilon_{\mathbf{k}n}$  in general. To correctly describe the spectral weight in multi-orbital systems, we use the retarded Green's function,

$$\begin{aligned} G_{\mathbf{k}mn}^R(\omega) &= (\omega + i\epsilon - H^{\text{Wannier}}(\mathbf{k}))_{mn}^{-1} \\ &= (\omega + i\epsilon - U^{\mathbf{k}} H^{\text{band}}(\mathbf{k}) U^{\mathbf{k}\dagger})_{mn}^{-1} \\ &= \sum_{\alpha} U_{m\alpha}^{\mathbf{k}} \frac{1}{\omega + i\epsilon - \epsilon_{\mathbf{k}\alpha}} (U_{n\alpha}^{\mathbf{k}})^*. \end{aligned} \quad (\text{A6})$$

The spectral function in multi-orbital systems is given by the imaginary part of the retarded Green's function,

$$A_{nn}(\mathbf{k}, \omega) = -\frac{1}{\pi} \text{Im} G_{\mathbf{k}nn}^R(\omega) = \sum_{\alpha} |U_{n\alpha}^{\mathbf{k}}|^2 \delta(\omega - \epsilon_{\mathbf{k}\alpha}). \quad (\text{A7})$$

Then, the spectral weight of orbital  $n$  at the Fermi energy is given by

$$w_{\mathbf{k}n} = A_{nn}(\mathbf{k}, \epsilon_F) = \sum_{\alpha} |U_{n\alpha}^{\mathbf{k}}|^2 \delta(\epsilon_{\mathbf{k}\alpha} - \epsilon_F). \quad (\text{A8})$$

If the off-diagonal components in the Wannier basis are absent, and if one chooses the ordering of band indices to match the orbital indices, the unitary matrix becomes identity,  $U_{n\alpha}^{\mathbf{k}} = \delta_{n\alpha}$ , and the weight becomes  $w_{\mathbf{k}n} = \delta(\epsilon_{\mathbf{k}n} - \epsilon_F)$ . The density of states at the Fermi energy for orbital  $n$  is given by

$$D(\epsilon_F) = \frac{1}{N_{\mathbf{k}}} \sum_{\mathbf{k}} w_{\mathbf{k}n} = \frac{1}{N_{\mathbf{k}}} \sum_{\mathbf{k}} A_{nn}(\mathbf{k}, \epsilon_F) = \frac{1}{N_{\mathbf{k}}} \sum_{\mathbf{k}\alpha} |U_{n\alpha}^{\mathbf{k}}|^2 \delta(\epsilon_{\mathbf{k}\alpha} - \epsilon_F). \quad (\text{A9})$$

In the case of NbN, the density of states does not depend on  $n$  due to the reason stated above.

Using the general expression of the spectral weight  $w_{\mathbf{k}n}$  (A8), the Fermi surface average of the effective interaction is defined by

$$\langle V_{mn} \rangle_{\text{FS}} = \frac{\sum_{\mathbf{k}, \mathbf{q}} w_{\mathbf{k}+q\mathbf{m}} w_{\mathbf{k}n} V_{mn}(\mathbf{k}, \mathbf{q})}{\sum_{\mathbf{k}, \mathbf{q}} w_{\mathbf{k}+q\mathbf{m}} w_{\mathbf{k}n}}. \quad (\text{A10})$$

This definition can be obtained by simply replacing the delta functions in Eq. (A1) with  $w_{\mathbf{k}n}$ . By using the density of states (A9) and assuming that the density of states does not depend on orbitals, we arrive at

$$\langle V_{mn} \rangle_{\text{FS}} = \frac{1}{N_{\mathbf{k}} N_{\mathbf{q}}} \sum_{\mathbf{k}, \mathbf{q}} \frac{w_{\mathbf{k}+q\mathbf{m}} w_{\mathbf{k}n}}{D^2(\epsilon_F)} V_{mn}(\mathbf{k}, \mathbf{q}). \quad (\text{A11})$$

This is the general expression for the Fermi-surface-averaged effective interaction that we showed as Eq. (6) in the main text. In our calculations, we find that NbN has very small off-diagonal hoppings, where Eqs. (A11) and (A1) are almost equivalent. Even in this case, however, it is safe to use Eq. (A11) since the ordering of the orbital indices may be shuffled at various  $\mathbf{k}$  points (so that it becomes tiresome to track the label ordering) and in the vicinity of degenerate points ( $\epsilon_{\mathbf{k}m} \approx \epsilon_{\mathbf{k}n}$  for  $m \neq n$ ) off-diagonal components may not be neglected.

## Appendix B: THG susceptibilities for disordered multiband superconductors

In this Appendix, we present the detailed formulation of THG susceptibilities for disordered multiband superconductors within the BCS mean-field and self-consistent Born approximations. The basic idea of the derivation has been given in Sec. III in the main text. We differentiate the Green's function, the self-energy, and the superconducting gap with respect to the external field, and determine the second-order derivatives,  $\hat{G}_{\mathbf{k}n}^{\ddot{}}$  (17),  $\hat{\Sigma}_n^{\ddot{}}$  (18), and  $\hat{\Delta}_n^{\ddot{}}$  (19), in the self-consistent manner.

To this end, we first determine the  $\tau_1$  vertex function  $\hat{\Lambda}_{mn}^{\tau_1}(\omega; \Omega)$ , which is the  $\tau_1$  vertex dressed by the impurity-ladder corrections, satisfying the Bethe-Salpeter equation,

$$\hat{\Lambda}_{mn}^{\tau_1}(\omega; \Omega) = \hat{\tau}_1 \delta_{mn} + \sum_l \gamma_{ml}^2 \frac{1}{N_{\mathbf{k}}} \sum_{\mathbf{k}} \hat{\tau}_3 \hat{G}_{\mathbf{k}l}(\omega + 2\Omega) \hat{\Lambda}_{ln}^{\tau_1}(\omega; \Omega) \hat{G}_{\mathbf{k}l}(\omega) \hat{\tau}_3, \quad (\text{B1})$$

where we omit the superscript  $\alpha = R, A, <$ . We also have the Bethe-Salpeter equations for the diamagnetic and paramagnetic vertex functions  $\hat{\Lambda}_n^{\text{dia}}(\mathbf{k}, \omega; \Omega)$  and  $\hat{\Lambda}_n^{\text{para}}(\mathbf{k}, \omega; \Omega)$ ,

$$\hat{\Lambda}_n^{\text{dia}}(\mathbf{k}, \omega; \Omega) = \hat{\epsilon}_{\mathbf{k}n} \hat{\tau}_3 + \sum_m \gamma_{nm}^2 \frac{1}{N_{\mathbf{k}}} \sum_{\mathbf{k}} \hat{\tau}_3 \hat{G}_{\mathbf{k}m}(\omega + 2\Omega) \hat{\Lambda}_m^{\text{dia}}(\mathbf{k}, \omega; \Omega) \hat{G}_{\mathbf{k}m}(\omega) \hat{\tau}_3, \quad (\text{B2})$$

$$\hat{\Lambda}_n^{\text{para}}(\mathbf{k}, \omega; \Omega) = 2\hat{\epsilon}_{\mathbf{k}n} \hat{G}_{\mathbf{k}n}(\omega + \Omega) \hat{\epsilon}_{\mathbf{k}n} + \sum_m \gamma_{nm}^2 \frac{1}{N_{\mathbf{k}}} \sum_{\mathbf{k}} \hat{\tau}_3 \hat{G}_{\mathbf{k}m}(\omega + 2\Omega) \hat{\Lambda}_m^{\text{para}}(\mathbf{k}, \omega; \Omega) \hat{G}_{\mathbf{k}m}(\omega) \hat{\tau}_3. \quad (\text{B3})$$

One can decouple the momentum dependence of the diamagnetic and paramagnetic vertex functions as

$$\hat{\Lambda}_n^{\text{dia}}(\mathbf{k}, \omega; \Omega) = \hat{\epsilon}_{\mathbf{k}n} \hat{\tau}_3 + \hat{\Lambda}_n^{\text{dia}}(\omega; \Omega), \quad (\text{B4})$$

$$\hat{\Lambda}_n^{\text{para}}(\mathbf{k}, \omega; \Omega) = 2\hat{\epsilon}_{\mathbf{k}n} \hat{G}_{\mathbf{k}n}(\omega + \Omega) \hat{\epsilon}_{\mathbf{k}n} + \hat{\Lambda}_n^{\text{para}}(\omega; \Omega). \quad (\text{B5})$$

We solve the self-consistent equations (B1), (B2), and (B3) for  $\hat{\Lambda}_{mn}^{\tau_1}(\omega; \Omega)$ ,  $\hat{\Lambda}_n^{\text{dia}}(\omega; \Omega)$ , and  $\hat{\Lambda}_n^{\text{para}}(\omega; \Omega)$  numerically by matrix inversion. After that, we substitute them to the following self-consistent equations for the second-order



derivatives of the superconducting gap function in the diamagnetic and paramagnetic channels,

$$\ddot{\Delta}_n^{\text{dia}}(\Omega) = \frac{i}{2} \sum_m V_{nm} \int \frac{d\omega}{2\pi} \frac{1}{N_{\mathbf{k}}} \sum_{\mathbf{k}} \text{Tr} \left[ \hat{\tau}_1 \hat{G}_{\mathbf{k}m}(\omega + 2\Omega) \left( \hat{\Lambda}_m^{\text{dia}}(\mathbf{k}, \omega; \Omega) + \sum_l \hat{\Lambda}_{ml}^{\tau_1}(\omega; \Omega) \ddot{\Delta}_l^{\text{dia}}(\Omega) \right) \hat{G}_{\mathbf{k}m}(\omega) \right]^{<}, \quad (\text{B6})$$

$$\ddot{\Delta}_n^{\text{para}}(\Omega) = \frac{i}{2} \sum_m V_{nm} \int \frac{d\omega}{2\pi} \frac{1}{N_{\mathbf{k}}} \sum_{\mathbf{k}} \text{Tr} \left[ \hat{\tau}_1 \hat{G}_{\mathbf{k}m}(\omega + 2\Omega) \left( \hat{\Lambda}_m^{\text{para}}(\mathbf{k}, \omega; \Omega) + \sum_l \hat{\Lambda}_{ml}^{\tau_1}(\omega; \Omega) \ddot{\Delta}_l^{\text{para}}(\Omega) \right) \hat{G}_{\mathbf{k}m}(\omega) \right]^{<}, \quad (\text{B7})$$

which are again solved numerically by matrix inversion.

Finally, the THG susceptibility is determined from the vertex functions. The classification of the THG susceptibility in terms of the diagrammatic topology has been given in Table II. The explicit expressions for the quasiparticle contributions to the THG in each channel are given by

$$\chi_{\text{qp}}^{(1)}(\Omega) = \frac{i}{6} \int \frac{d\omega}{2\pi} \frac{1}{N_{\mathbf{k}}} \sum_{\mathbf{k}n} \text{Tr}[\ddot{\epsilon}_{\mathbf{k}n} \hat{\tau}_3 \hat{G}_{\mathbf{k}n}(\omega)]^{<}, \quad (\text{B8})$$

$$\chi_{\text{qp}}^{(2)}(\Omega) = \frac{i}{2} \int \frac{d\omega}{2\pi} \frac{1}{N_{\mathbf{k}}} \sum_{\mathbf{k}n} \text{Tr}[\ddot{\epsilon}_{\mathbf{k}n} \hat{G}_{\mathbf{k}n}(\omega + \Omega) \dot{\epsilon}_{\mathbf{k}n} \hat{G}_{\mathbf{k}n}(\omega)]^{<} + \frac{i}{6} \int \frac{d\omega}{2\pi} \frac{1}{N_{\mathbf{k}}} \sum_{\mathbf{k}n} \text{Tr}[\dot{\epsilon}_{\mathbf{k}n} \hat{G}_{\mathbf{k}n}(\omega + 3\Omega) \ddot{\epsilon}_{\mathbf{k}n} \hat{G}_{\mathbf{k}n}(\omega)]^{<}, \quad (\text{B9})$$

$$\begin{aligned} \chi_{\text{qp}}^{(3)}(\Omega) &= \frac{i}{2} \int \frac{d\omega}{2\pi} \frac{1}{N_{\mathbf{k}}} \sum_{\mathbf{k}n} \text{Tr}[\ddot{\epsilon}_{\mathbf{k}n} \hat{\tau}_3 \hat{G}_{\mathbf{k}n}(\omega + 2\Omega) \dot{\epsilon}_{\mathbf{k}n} \hat{\tau}_3 \hat{G}_{\mathbf{k}n}(\omega)]^{<} \\ &+ \frac{i}{2} \int \frac{d\omega}{2\pi} \frac{1}{N_{\mathbf{k}}} \sum_{\mathbf{k}n} \text{Tr}[\dot{\epsilon}_{\mathbf{k}n} \hat{\tau}_3 \hat{G}_{\mathbf{k}n}(\omega + 2\Omega) \hat{\Lambda}_n^{\text{dia}}(\omega; \Omega) \hat{G}_{\mathbf{k}n}(\omega)]^{<}, \end{aligned} \quad (\text{B10})$$

$$\begin{aligned} \chi_{\text{qp}}^{(4)}(\Omega) &= i \int \frac{d\omega}{2\pi} \frac{1}{N_{\mathbf{k}}} \sum_{\mathbf{k}n} \text{Tr}[\dot{\epsilon}_{\mathbf{k}n} \hat{\tau}_3 \hat{G}_{\mathbf{k}n}(\omega + 2\Omega) \dot{\epsilon}_{\mathbf{k}n} \hat{G}_{\mathbf{k}n}(\omega + \Omega) \dot{\epsilon}_{\mathbf{k}n} \hat{G}_{\mathbf{k}n}(\omega)]^{<} \\ &+ \frac{i}{2} \int \frac{d\omega}{2\pi} \frac{1}{N_{\mathbf{k}}} \sum_{\mathbf{k}n} \text{Tr}[\dot{\epsilon}_{\mathbf{k}n} \hat{G}_{\mathbf{k}n}(\omega + 3\Omega) \dot{\epsilon}_{\mathbf{k}n} \hat{G}_{\mathbf{k}n}(\omega + 2\Omega) \ddot{\epsilon}_{\mathbf{k}n} \hat{\tau}_3 \hat{G}_{\mathbf{k}n}(\omega)]^{<} \\ &+ \frac{i}{2} \int \frac{d\omega}{2\pi} \frac{1}{N_{\mathbf{k}}} \sum_{\mathbf{k}n} \text{Tr}[\dot{\epsilon}_{\mathbf{k}n} \hat{G}_{\mathbf{k}n}(\omega + 3\Omega) \ddot{\epsilon}_{\mathbf{k}n} \hat{\tau}_3 \hat{G}_{\mathbf{k}n}(\omega + \Omega) \dot{\epsilon}_{\mathbf{k}n} \hat{G}_{\mathbf{k}n}(\omega)]^{<} \\ &+ i \int \frac{d\omega}{2\pi} \frac{1}{N_{\mathbf{k}}} \sum_{\mathbf{k}n} \text{Tr}[\ddot{\epsilon}_{\mathbf{k}n} \hat{\tau}_3 \hat{G}_{\mathbf{k}n}(\omega + 2\Omega) \hat{\Lambda}_n^{\text{para}}(\omega; \Omega) \hat{G}_{\mathbf{k}n}(\omega)]^{<} \\ &+ \frac{i}{2} \int \frac{d\omega}{2\pi} \frac{1}{N_{\mathbf{k}}} \sum_{\mathbf{k}n} \text{Tr}[\dot{\epsilon}_{\mathbf{k}n} \hat{G}_{\mathbf{k}n}(\omega + 3\Omega) \dot{\epsilon}_{\mathbf{k}n} \hat{G}_{\mathbf{k}n}(\omega + 2\Omega) \hat{\Lambda}_n^{\text{dia}}(\omega; \Omega) \hat{G}_{\mathbf{k}n}(\omega)]^{<} \\ &+ \frac{i}{2} \int \frac{d\omega}{2\pi} \frac{1}{N_{\mathbf{k}}} \sum_{\mathbf{k}n} \text{Tr}[\dot{\epsilon}_{\mathbf{k}n} \hat{G}_{\mathbf{k}n}(\omega + 3\Omega) \hat{\Lambda}_n^{\text{dia}}(\omega + \Omega; \Omega) \hat{G}_{\mathbf{k}n}(\omega + \Omega) \dot{\epsilon}_{\mathbf{k}n} \hat{G}_{\mathbf{k}n}(\omega)]^{<}, \end{aligned} \quad (\text{B11})$$

$$\begin{aligned} \chi_{\text{qp}}^{(5)}(\Omega) &= i \int \frac{d\omega}{2\pi} \frac{1}{N_{\mathbf{k}}} \sum_{\mathbf{k}n} \text{Tr}[\dot{\epsilon}_{\mathbf{k}n} \hat{G}_{\mathbf{k}n}(\omega + 3\Omega) \dot{\epsilon}_{\mathbf{k}n} \hat{G}_{\mathbf{k}n}(\omega + 2\Omega) \dot{\epsilon}_{\mathbf{k}n} \hat{G}_{\mathbf{k}n}(\omega + \Omega) \dot{\epsilon}_{\mathbf{k}n} \hat{G}_{\mathbf{k}n}(\omega)]^{<} \\ &+ i \int \frac{d\omega}{2\pi} \frac{1}{N_{\mathbf{k}}} \sum_{\mathbf{k}n} \text{Tr}[\dot{\epsilon}_{\mathbf{k}n} \hat{G}_{\mathbf{k}n}(\omega + 3\Omega) \dot{\epsilon}_{\mathbf{k}n} \hat{G}_{\mathbf{k}n}(\omega + 2\Omega) \hat{\Lambda}_n^{\text{para}}(\omega; \Omega) \hat{G}_{\mathbf{k}n}(\omega)]^{<} \\ &+ i \int \frac{d\omega}{2\pi} \frac{1}{N_{\mathbf{k}}} \sum_{\mathbf{k}n} \text{Tr}[\dot{\epsilon}_{\mathbf{k}n} \hat{G}_{\mathbf{k}n}(\omega + 3\Omega) \hat{\Lambda}_n^{\text{para}}(\omega + \Omega; \Omega) \hat{G}_{\mathbf{k}n}(\omega + \Omega) \dot{\epsilon}_{\mathbf{k}n} \hat{G}_{\mathbf{k}n}(\omega)]^{<}. \end{aligned} \quad (\text{B12})$$

The expressions for the Higgs-mode contributions are given by

$$\chi_H^{(1)}(\Omega) = \frac{i}{2} \int \frac{d\omega}{2\pi} \frac{1}{N_{\mathbf{k}}} \sum_{\mathbf{k}n} \text{Tr}[\ddot{\epsilon}_{\mathbf{k}n} \hat{\tau}_3 \hat{G}_{\mathbf{k}n}(\omega + 2\Omega) \ddot{\Delta}_n^{\text{dia}}(\Omega) \hat{\tau}_1 \hat{G}_{\mathbf{k}n}(\omega)]^<, \quad (\text{B13})$$

$$\begin{aligned} \chi_H^{(2)}(\Omega) &= \frac{i}{2} \int \frac{d\omega}{2\pi} \frac{1}{N_{\mathbf{k}}} \sum_{\mathbf{k}n} \text{Tr}[\ddot{\epsilon}_{\mathbf{k}n} \hat{\tau}_3 \hat{G}_{\mathbf{k}n}(\omega + 2\Omega) \ddot{\Delta}_n^{\text{para}}(\Omega) \hat{\tau}_1 \hat{G}_{\mathbf{k}n}(\omega)]^< \\ &+ \frac{i}{2} \int \frac{d\omega}{2\pi} \frac{1}{N_{\mathbf{k}}} \sum_{\mathbf{k}n} \text{Tr}[\dot{\epsilon}_{\mathbf{k}n} \hat{G}_{\mathbf{k}n}(\omega + 3\Omega) \dot{\epsilon}_{\mathbf{k}n} \hat{G}_{\mathbf{k}n}(\omega + 2\Omega) \ddot{\Delta}_n^{\text{dia}}(\Omega) \hat{\tau}_1 \hat{G}_{\mathbf{k}n}(\omega)]^< \\ &+ \frac{i}{2} \int \frac{d\omega}{2\pi} \frac{1}{N_{\mathbf{k}}} \sum_{\mathbf{k}n} \text{Tr}[\dot{\epsilon}_{\mathbf{k}n} \hat{G}_{\mathbf{k}n}(\omega + 3\Omega) \ddot{\Delta}_n^{\text{dia}}(\Omega) \hat{\tau}_1 \hat{G}_{\mathbf{k}n}(\omega + \Omega) \dot{\epsilon}_{\mathbf{k}n} \hat{G}_{\mathbf{k}n}(\omega)]^<, \end{aligned} \quad (\text{B14})$$

$$\begin{aligned} \chi_H^{(3)}(\Omega) &= \frac{i}{2} \int \frac{d\omega}{2\pi} \frac{1}{N_{\mathbf{k}}} \sum_{\mathbf{k}n} \text{Tr}[\dot{\epsilon}_{\mathbf{k}n} \hat{G}_{\mathbf{k}n}(\omega + 3\Omega) \dot{\epsilon}_{\mathbf{k}n} \hat{G}_{\mathbf{k}n}(\omega + 2\Omega) \ddot{\Delta}_n^{\text{para}}(\Omega) \hat{\tau}_1 \hat{G}_{\mathbf{k}n}(\omega)]^< \\ &+ \frac{i}{2} \int \frac{d\omega}{2\pi} \frac{1}{N_{\mathbf{k}}} \sum_{\mathbf{k}n} \text{Tr}[\dot{\epsilon}_{\mathbf{k}n} \hat{G}_{\mathbf{k}n}(\omega + 3\Omega) \ddot{\Delta}_n^{\text{para}}(\Omega) \hat{\tau}_1 \hat{G}_{\mathbf{k}n}(\omega + \Omega) \dot{\epsilon}_{\mathbf{k}n} \hat{G}_{\mathbf{k}n}(\omega)]^<. \end{aligned} \quad (\text{B15})$$

- 
- [1] P. W. Anderson, “Random-Phase Approximation in the Theory of Superconductivity,” *Phys. Rev.* **112**, 1900 (1958).
- [2] A. Schmid, “The Approach to Equilibrium in a Pure Superconductor: The Relaxation of the Cooper Pair Density,” *Phys. Kondens. Mater.* **8**, 129 (1968).
- [3] A. F. Volkov and S. M. Kogan, “Collisionless relaxation of the energy gap in superconductors”, *Sov. Phys. JETP* **38**, 1018 (1974).
- [4] I. O. Kulik, O. Entin-Wohlman, and R. Orbach, “Pair susceptibility and mode propagation in superconductors: A microscopic approach,” *J. Low Temp. Phys.* **43**, 591 (1981).
- [5] P. B. Littlewood and C. M. Varma, “Gauge-Invariant Theory of the Dynamical Interaction of Charge Density Waves and Superconductivity,” *Phys. Rev. Lett.* **47**, 811 (1981).
- [6] P. B. Littlewood and C. M. Varma, “Amplitude collective modes in superconductors and their coupling to charge-density waves,” *Phys. Rev. B* **26**, 4883 (1982).
- [7] D. Pekker and C. M. Varma, “Amplitude/Higgs Modes in Condensed Matter Physics,” *Annu. Rev. Condens. Matter Phys.* **6**, 269 (2015).
- [8] R. Shimano and N. Tsuji, “Higgs Mode in Superconductors,” *Annu. Rev. Condens. Matter Phys.* **11**, 103 (2020).
- [9] R. Sooryakumar and M. V. Klein, “Raman Scattering by Superconducting-Gap Excitations and Their Coupling to Charge-Density Waves,” *Phys. Rev. Lett.* **45**, 660 (1980).
- [10] R. Sooryakumar and M. V. Klein, “Raman scattering from superconducting gap excitations in the presence of a magnetic field,” *Phys. Rev. B* **23**, 3213 (1981).
- [11] M.-A. Méasson, Y. Gallais, M. Cazayous, B. Clair, P. Rodière, L. Cario, and A. Sacuto, “Amplitude Higgs mode in the  $2H - \text{NbSe}_2$  superconductor,” *Phys. Rev. B* **89**, 060503 (2014).
- [12] R. Grasset, T. Cea, Y. Gallais, M. Cazayous, A. Sacuto, L. Cario, L. Benfatto, and M.-A. Méasson, “Higgs-mode radiance and charge-density-wave order in  $2H - \text{NbSe}_2$ ,” *Phys. Rev. B* **97**, 094502 (2018).
- [13] R. Grasset, Y. Gallais, A. Sacuto, M. Cazayous, S. Mañas Valero, E. Coronado, and M.-A. Méasson, “Pressure-Induced Collapse of the Charge Density Wave and Higgs Mode Visibility in  $2H - \text{TaS}_2$ ,” *Phys. Rev. Lett.* **122**, 127001 (2019).
- [14] N. Tsuji and H. Aoki, “Theory of Anderson pseudospin resonance with Higgs mode in superconductors,” *Phys. Rev. B* **92**, 064508 (2015).
- [15] R. Matsunaga, Y. I. Hamada, K. Makise, Y. Uzawa, H. Terai, Z. Wang, and R. Shimano, “Higgs Amplitude Mode in the BCS Superconductors  $\text{Nb}_{1-x}\text{Ti}_x\text{N}$  Induced by Terahertz Pulse Excitation,” *Phys. Rev. Lett.* **111**, 057002 (2013).
- [16] R. Matsunaga, N. Tsuji, H. Fujita, A. Sugioka, K. Makise, Y. Uzawa, H. Terai, Z. Wang, H. Aoki, and R. Shimano, “Light-induced collective pseudospin precession resonating with Higgs mode in a superconductor,” *Science* **345**, 1145 (2014).
- [17] T. Cea, C. Castellani, and L. Benfatto, “Nonlinear optical effects and third-harmonic generation in superconductors: Cooper pairs versus Higgs mode contribution,” *Phys. Rev. B* **93**, 180507 (2016).
- [18] R. Matsunaga, N. Tsuji, K. Makise, H. Terai, H. Aoki, and R. Shimano, “Polarization-resolved terahertz third-harmonic generation in a single-crystal superconductor NbN: Dominance of the Higgs mode beyond the BCS approximation,” *Phys. Rev. B* **96**, 020505 (2017).
- [19] K. E. Kihlstrom, R. W. Simon, and S. A. Wolf, “Tunneling  $\alpha^2 F(\omega)$  from sputtered thin-film NbN,” *Phys. Rev. B* **32**, 1843 (1985).
- [20] S. D. Brorson, A. Kazeroonian, J. S. Moodera, D. W. Face, T. K. Cheng, E. P. Ippen, M. S. Dresselhaus, and G. Dresselhaus, “Femtosecond room-temperature measurement of the electron-phonon coupling constant  $\gamma$  in metallic superconductors,” *Phys. Rev. Lett.* **64**, 2172 (1990).
- [21] S. P. Chockalingam, M. Chand, J. Jesudasan, V. Tri-

- pathi, and P. Raychaudhuri, “Superconducting properties and Hall effect of epitaxial NbN thin films,” *Phys. Rev. B* **77**, 214503 (2008).
- [22] H. Aoki, N. Tsuji, M. Eckstein, M. Kollar, T. Oka, and P. Werner, “Nonequilibrium dynamical mean-field theory and its applications,” *Rev. Mod. Phys.* **86**, 779 (2014).
- [23] N. Tsuji, Y. Murakami, and H. Aoki, “Nonlinear light-Higgs coupling in superconductors beyond BCS: Effects of the retarded phonon-mediated interaction,” *Phys. Rev. B* **94**, 224519 (2016).
- [24] D. C. Mattis and J. Bardeen, “Theory of the Anomalous Skin Effect in Normal and Superconducting Metals,” *Phys. Rev.* **111**, 412 (1958).
- [25] T. Jujo, “Quasiclassical Theory on Third-Harmonic Generation in Conventional Superconductors with Paramagnetic Impurities,” *J. Phys. Soc. Jpn.* **87**, 024704 (2018).
- [26] Y. Murotani and R. Shimano, “Nonlinear optical response of collective modes in multiband superconductors assisted by nonmagnetic impurities,” *Phys. Rev. B* **99**, 224510 (2019).
- [27] M. Silaev, “Nonlinear electromagnetic response and Higgs-mode excitation in BCS superconductors with impurities,” *Phys. Rev. B* **99**, 224511 (2019).
- [28] T. Cea, P. Barone, C. Castellani, and L. Benfatto, “Polarization dependence of the third-harmonic generation in multiband superconductors,” *Phys. Rev. B* **97**, 094516 (2018).
- [29] L. F. Mattheiss, “Electronic Band Structure of Niobium Nitride,” *Phys. Rev. B* **5**, 315 (1972).
- [30] C. Y. Fong and M. L. Cohen, “Pseudopotential Calculations of the Electronic Structure of a Transition-Metal Compound-Niobium Nitride,” *Phys. Rev. B* **6**, 3633 (1972).
- [31] D. J. Chadi and M. L. Cohen, “Electronic band structures and charge densities of NbC and NbN,” *Phys. Rev. B* **10**, 496 (1974).
- [32] T. Amriou, B. Bouhafs, H. Aourag, B. Khelifa, S. Bresson, and C. Mathieu, “FP-LAPW investigations of electronic structure and bonding mechanism of NbC and NbN compounds,” *Physica B* **325**, 46 (2003).
- [33] D. A. Papaconstantopoulos, W. E. Pickett, B. M. Klein, and L. L. Boyer, “Electronic properties of transition-metal nitrides: The group-V and group-VI nitrides VN, NbN, TaN, CrN, MoN, and WN,” *Phys. Rev. B* **31**, 752 (1985).
- [34] E. I. Isaev, R. Ahuja, S. I. Simak, A. I. Lichtenstein, Yu. Kh. Vekilov, B. Johansson, and I. A. Abrikosov, “Anomalously enhanced superconductivity and ab initio lattice dynamics in transition metal carbides and nitrides,” *Phys. Rev. B* **72**, 064515 (2005).
- [35] E. I. Isaev, S. I. Simak, I. A. Abrikosov, R. Ahuja, Yu. Kh. Vekilov, M. I. Katsnelson, A. I. Lichtenstein, and B. Johansson, “Phonon related properties of transition metals, their carbides, and nitrides: A first-principles study,” *J. Appl. Phys.* **101**, 123519 (2007).
- [36] S. Blackburn, M. Côté, S. G. Louie, and M. L. Cohen, “Enhanced electron-phonon coupling near the lattice instability of superconducting  $\text{NbC}_{1-x}\text{N}_x$  from density-functional calculations,” *Phys. Rev. B* **84**, 104506 (2011).
- [37] P. Giannozzi et al., “QUANTUM ESPRESSO: a modular and open-source software project for quantum simulations of materials,” *J. Phys.: Condens. Matter* **21**, 395502 (2009).
- [38] P. Giannozzi et al., “Advanced capabilities for materials modelling with quantum ESPRESSO,” *J. Phys.: Condens. Matter* **29**, 465901 (2017).
- [39] N. Troullier and J. L. Martins, “Efficient pseudopotentials for plane-wave calculations,” *Phys. Rev. B* **43**, 1993 (1991).
- [40] L. Kleinman and D. M. Bylander, “Efficacious Form for Model Pseudopotentials,” *Phys. Rev. Lett.* **48**, 1425 (1982).
- [41] J. P. Perdew, K. Burke, and M. Ernzerhof, “Generalized Gradient Approximation Made Simple,” *Phys. Rev. Lett.* **77**, 3865 (1996).
- [42] S. Baroni, S. de Gironcoli, A. Dal Corso, and P. Giannozzi, “Phonons and related crystal properties from density-functional perturbation theory,” *Rev. Mod. Phys.* **73**, 515 (2001).
- [43] G. Heger and O. Baumgartner, “Crystal structure and lattice distortion of  $\gamma\text{-NbN}_x$  and  $\delta\text{-NbN}_x$ ,” *J. Phys. C: Solid State Phys.* **13**, 5833 (1980).
- [44] N. Marzari and D. Vanderbilt, “Maximally localized generalized Wannier functions for composite energy bands,” *Phys. Rev. B* **56**, 12847 (1997).
- [45] I. Souza, N. Marzari, and D. Vanderbilt, “Maximally localized Wannier functions for entangled energy bands,” *Phys. Rev. B* **65**, 035109 (2001).
- [46] K. Nakamura, Y. Yoshimoto, Y. Nomura, T. Tadano, M. Kawamura, T. Kosugi, K. Yoshimi, T. Misawa, and Y. Motoyama, “RESPACK: An *ab initio* tool for derivation of effective low-energy model of material”, arXiv:2001.02351.
- [47] Y. Nomura, K. Nakamura, and R. Arita, “Effect of Electron-Phonon Interactions on Orbital Fluctuations in Iron-Based Superconductors,” *Phys. Rev. Lett.* **112**, 027002 (2014).
- [48] A. A. Abrikosov, L. P. Gorkov, and I. E. Dzyaloshinski, *Methods of Quantum Field Theory in Statistical Physics* (Dover, New York, 1975).
- [49] D. C. Langreth, “Linear and nonlinear response theory with applications”, in *Linear and Nonlinear Electron Transport in Solids*, edited by J. T. Devreese and V. E. van Doren (Plenum Press, New York, 1976).
- [50] P. W. Anderson, “Theory of dirty superconductors,” *J. Phys. Chem. Solids* **11**, 26 (1959).
- [51] T. Jujo, “Two-Photon Absorption by Impurity Scattering and Amplitude Mode in Conventional Superconductors,” *J. Phys. Soc. Jpn.* **84**, 114711 (2015).
- [52] R. V. Carlson and A. M. Goldman, “Superconducting Order-Parameter Fluctuations below  $T_c$ ,” *Phys. Rev. Lett.* **31**, 880 (1973).
- [53] R. V. Carlson and A. M. Goldman, “Propagating Order-Parameter Collective Modes in Superconducting Films,” *Phys. Rev. Lett.* **34**, 11 (1975).
- [54] A. J. Leggett, “Number-Phase Fluctuations in Two-Band Superconductors,” *Prog. Theor. Phys.* **36**, 901 (1966).
- [55] A. Akbari, A. P. Schnyder, D. Manske, and I. Eremin, “Theory of nonequilibrium dynamics of multiband superconductors,” *Europhys. Lett.* **101**, 17002 (2013).
- [56] H. Krull, N. Bittner, G. S. Uhrig, D. Manske, and A. P. Schnyder, “Coupling of Higgs and Leggett modes in nonequilibrium superconductors,” *Nat. Commun.* **7**, 11921 (2016).
- [57] Y. Murotani, N. Tsuji, and H. Aoki, “Theory of light-induced resonances with collective Higgs and Leggett modes in multiband superconductors,” *Phys. Rev. B* **95**, 104503 (2017).

- [58] Y. Barlas and C. M. Varma, “Amplitude or Higgs modes in  $d$ -wave superconductors,” *Phys. Rev. B* **87**, 054503 (2013).
- [59] K. Katsumi, N. Tsuji, Y. I. Hamada, R. Matsunaga, J. Schneeloch, R. D. Zhong, G. D. Gu, H. Aoki, Y. Gallais, and R. Shimano, “Higgs Mode in the  $d$ -Wave Superconductor  $\text{Bi}_2\text{Sr}_2\text{CaCu}_2\text{O}_{8+x}$  Driven by an Intense Terahertz Pulse,” *Phys. Rev. Lett.* **120**, 117001 (2018).
- [60] L. Schwarz, B. Fauseweh, N. Tsuji, N. Cheng, N. Bittner, H. Krull, M. Berciu, G. S. Uhrig, A. P. Schnyder, S. Kaiser, and D. Manske, “Classification and characterization of nonequilibrium Higgs modes in unconventional superconductors,” *Nat. Commun.* **11**, 287 (2020).
- [61] H. Chu, M.-J. Kim, K. Katsumi, S. Kovalev, R. D. Dawson, L. Schwarz, N. Yoshikawa, G. Kim, D. Putzky, Z. Z. Li, H. Raffy, S. Germanskiy, J.-C. Deinert, N. Awari, I. Ilyakov, B. Green, M. Chen, M. Bawatna, G. Cristiani, G. Logvenov, Y. Gallais, A. V. Boris, B. Keimer, A. P. Schnyder, D. Manske, M. Gensch, Z. Wang, R. Shimano, and S. Kaiser, “Phase-resolved Higgs response in superconducting cuprates,” *Nat. Commun.* **11**, 1793 (2020).
- [62] K. Katsumi, Z. Z. Li, H. Raffy, Y. Gallais, and R. Shimano, “Superconducting fluctuations probed by the Higgs mode in  $\text{Bi}_2\text{Sr}_2\text{CaCu}_2\text{O}_{8+x}$  thin films,” *Phys. Rev. B* **102**, 054510 (2020).
- [63] L. Schwarz and D. Manske, “Theory of driven Higgs oscillations and third-harmonic generation in unconventional superconductors,” *Phys. Rev. B* **101**, 184519 (2020).